IRAQI JOURNAL OF APPLIED PHYSICS

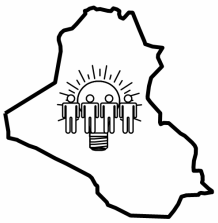

The *Iraqi Journal of Applied Physics (IJAP)* is a peer reviewed journal of high quality devoted to the publication of original research papers from applied physics and their broad range of applications. IJAP publishes quality original research papers, comprehensive review articles, survey articles, book reviews, dissertation abstracts in physics and its applications in the broadest sense. It is intended that the journal may act as an interdisciplinary forum for Physics and its applications. Innovative applications and material that brings together diverse areas of Physics are particularly welcome. Review articles in selected areas are published from time to time. It aims to disseminate knowledge; provide a learned reference in the field; and establish channels of communication between academic and research experts, policy makers and executives in industry, commerce and investment institutions. IJAP is a quarterly specialized periodical dedicated to publishing original papers, letters and reviews in: Applied & Nonlinear Optics, Applied Mechanics & Thermodynamics, Digital & Optical Communications, Electronic Materials & Devices, Laser Physics & Applications, Plasma Physics & Applications, Quantum Physics & Spectroscopy, Semiconductors & Optoelectronics, and Solid State Physics & Applications.

SPONSORED AND PUBLISHED BY
THE IRAQI SOCIETY FOR ALTERNATIVE AND RENEWABLE ENERGY SOURCES & TECHNIQUES (I.S.A.R.E.S.T.)

IRAQI JOURNAL OF APPLIED PHYSICS

" INSTRUCTIONS TO AUTHORS "

CONTRIBUTIONS

Contributions to be published in this journal should be original research works, i.e., those not already published or submitted for publication elsewhere, individual papers or letters to editor.
Manuscripts should be submitted to the editor at the mailing address:

Iraqi Journal of Applied Physics,
Editorial Board
P. O. Box 55259,
Baghdad 12001, IRAQ
submission@ijap.org **,** editor_ijap@yahoo.co.uk

MANUSCRIPTS

Two hard copies with soft copy on a compact disc (CD) should be submitted to Editor in the following configuration:

- Double-spaced one-side A4 size with 2.5 cm margins of all sides
- Times New Roman font (16pt bold for title, 14pt bold for names, 12pt bold for headings, 12pt regular for text)
- Letters should not exceed 10 pages, papers should not exceed 20 pages and reviews are up to author.
- Manuscripts presented in English only are accepted.
- English abstract not exceed 150 words
- 4 keywords (at least) should be maintained on (PACS preferred)
- Author(s) should express all quantities in SI units
- Equations should be written in equation form (*italic* and symbolic)
- Figures and Tables should be separated from text
- Figures and diagrams can be submitted in colors for assessment and they will be returned to authors after provide printable copies
- Charts should be indicated by the software used for
- Only original or high-resolution scanner photos are accepted
- For electronic submission, articles should be formatted with MS-Word software.

AUTHOR NAMES AND AFFILIATIONS

It is IJAP policy that all those who have participated significantly in the technical aspects of a paper be recognized as co-authors or cited in the acknowledgments. In the case of a paper with more than one author, correspondence concerning the paper will be sent to the first author unless staff is advised otherwise.
Author name should consist of first name, middle initial, last name. The author affiliation should consist of the following, as applicable, in the order noted:
- Company or college (with department name or company division), Postal address, City, state, zip code, Country name, and Telephone, and e-mail

REFERENCES

The references should be brought at the end of the article, and numbered in the order of their appearance in the paper. The reference list should be cited in accordance with the following examples:
[1] X. Ning and M.R. Lovell, "On the Sliding Friction Characteristics of Unidirectional Continuous FRP Composites", *ASME J. Tribol.*, 124(1) (2002) 5-13.
[2] M. Barnes, "Stresses in Solenoids", *J. Appl. Phys.*, 48(5) (2001) 2000–2008.
[3] J. Jones, "Contact Mechanics", Cambridge University Press (Cambridge, UK) (2000), Ch.6, p.56.
[4] Y. Lee, S.A. Korpela and R. Horne, "Structure of Multi-Cellular Natural Convection in a Tall Vertical Annulus", Proc. 7th International Heat Transfer Conference, U. Grigul et al., eds., Hemisphere (Washington DC), 2 (1982) 221–226.
[5] M. Hashish, "Waterjet Technology Development", High Pressure Technology, PVP-Vol. 406 (2000), 135-140.
[6] D.W. Watson, "Thermodynamic Analysis", ASME Paper No. 97-GT-288 (1997).
[7] C.Y. Tung, "Evaporative Heat Transfer in the Contact Line of a Mixture", Ph.D. thesis, Rensselaer Polytechnic Institute, Troy, NY (1982).

PROOFS

Authors will receive proofs of papers and are requested to return one corrected hard copy with a WORD copy on a compact disc (CD). New materials inserted in the original text without Editor permission may cause rejection of paper.

COPYRIGHT FORM

Author(s) will be asked to transfer copyrights of the article to the Journal soon after acceptance of it. This will ensure the widest possible dissemination of information.

OFFPRINTS

Authors will receive offprints free of charge and any additional offprints can be ordered.

SUBSCRIPTION AND ORDERS

Annual fees (4 issues per year) of subscription are:

- 50 US$ for individuals inside Iraq.
- 100 US$ for establishments inside Iraq.
- 100 US$ for individuals abroad.
- 200 US$ for establishments abroad.

Fees are reduced by 25% for I.S.A.R.E.S.T. members. Orders of issues can be submitted by contacting the editor-in-chief or editorial office at **subscription@ijap.org** to maintain the address of issue delivery and payment way.

Empirical and Simulation of Thermal Insulator of SWCNTs – Ceramic/Polymer Nanocomposites

Itab F. Hussen

Department of Physics, College of Science, Al- Mustansiriya University, Baghdad, IRAQ

Ablation rate and thermal conductivity coefficient for phenol formaldehyde type resole resin reinforced with single well carbon nanotubes (SWCNTs) and porcelain have been studied via oxy–acetylene flame and Lee's disc, techniques respectively. Thermal conductivity results show, that the values increase progressively by succession of volume fraction of SWCNTs. Ablation rate behaves inversely, where it drops at high volume fraction of SWCNTs. Simulation of thermal conductivity results, which are calculated according to microstructures model and when we compared it, with the experimental results, it can be observed, that the experimental results, were located in between the parallel direction values and random direction values for SWCNTs, with respect to heat flux direction. Ablation simulation results values coming higher than experimental results values, this could be explained, as the interface affect of nanocomposites, which had high strength and strong bond force.

Keywords: Ablation, Thermal conductivity, Porcelain, Nanocomposites
Received: 1 June 2011, **Revised**: 24 September 2011, **Accepted**: 1 October 2011

1. Introduction

Polymer nanocomposites (PNCs) are a rapidly growing area of nanoengineered materials, providing lighter weight alternatives to conventional, filled polymers with additional functionality associated with nanoscale specific, value-added properties. If the promise and excitement surrounding layered porcelain and carbon nanotubes are any indication, the future of PNC technology is truly boundless. The opportunities to extend PNC concepts to other nanoelements and polymer hosts are immense, opening the way to provide tailor-made materials that circumvent current limitations.

By adding fillers, such as minerals, ceramics, metals, or even air, material scientists can generate an infinite variety of materials with unique physical properties and competitive production costs. For example, adding filler to a commodity thermoset such as resole can achieve performance levels that would otherwise require a much more expensive engineering polymer. Similarly, combining different polymers to form a polymer blend or resin can increase the value of existing polymers.

Polymer nanocomposites incorporate a new spectrum of fillers that extend the function and utility of polymers while maintaining the manufacturing and processing flexibility inherent to plastics, thermosets, and resins. In particular, polymer nanocomposites have been successful with regard to overcoming traditionally antagonistic combinations of properties [1].

Since the first reports in the late 1980s [2-7] the term "polymer nanocomposite" has evolved to refer to a multi component system in which the major constituent is a polymer or blend thereof and the minor constituent has at least one dimension below 100 nm. Polymer nanocomposite is an appropriate synonym for inorganic–organic hybrids and molecular composites and also encompasses mature commercial products such as polymers containing carbon black or fumed silica.

When fillers are nanoscopic, there are advantages afforded to filled polymers and composites that lead to performance enhancements. These advantages result primarily from filler size reduction and the concomitant increase in surface area. The size of the additive might drop by up to three orders of magnitude relative to conventional alternatives. In contrast, many nanotechnologies associated with electrical or thermal properties benefit from new physical phenomena arising from quantum confinement effects induced by the nanoscale dimensions of the material. The literatures about polymer nanocomposites contains many discussions about the implications and physical manifestations of the reduction in filler length scale [8-12].

Many of modern technologies require materials with unusual combinations of properties that cannot be met by the conventional metal alloys, ceramics and polymeric materials. This is especially true for materials that are needed for aerospace, under water and transportation applications [13]. Ceramics display a variety of useful electrical, thermal and magnetic properties, and it is one of the important thermal insulators [14]. In the last forty years of the last century a great deal of assessment has been carried out in the manufacturing of thermal

insulators. Bauer and Dietz discussed the future needs for porcelain insulators [15]. Two important applications, for ceramics materials, include thermal insulators and refractories. Ceramic insulators (more commonly, porcelain insulator) occupy vital area of these field; porcelain is the material made of mixture of various white – burning clays and fluxes of such a nature and in such properties as will produce a dense and vitreous body.

Ablation phenomena is defined as; the degradation, decomposition, and erosion of a material caused by high temperature, pressure, time, percent oxidizing species, and velocity of gas flow a controlled loss of material to protect the underlying structure. Also, ablative plastic, is defined as; a material that absorbs heat (with a low material loss and char rate) through a decomposition process (pyrolysis) that takes place at or near the surface exposed to the heat [16]. The phenolic resins are made from phenols and formaldehyde. The resoles are prepared under alkaline conditions with formaldehyde/phenol (F/P) ratios greater than one. Resoles are cured by applying heat and /or by adding acids. The phenolics are rated for good resistance to high temperature, good thermal stability, and low smoke generation [17]. The theoretical simulation of ablative test of a thermal insulator is considered as an important process since it reduces many efforts, time and raw materials that are used in trail and error of the experimental procedure. This simulation is performed by using the values of thermal parameters of the specific material. Although this simulation is sometimes difficult to perform because of time and programming difficulties on personal computers, some approximations can result in reasonable results. Two methods are usually used for this simulation, finite element and finite difference methods. The two methods are adequate for the simulation, however finite difference method (FDM) needs more computing time to reach the accuracy of finite element method (FEM). This is opposed with simple formulation of FDM with respect to FEM. This method is useful in inspecting thermal protection of buildings, instruments and other situations where thermal insulation is important. This simulation is also important in investigating the shape, speed, temperature and rate of ablation [18].

2. Theoretical Approach

Heat transfer can be described as the energy transfer from one system to another as a result of temperature difference. It occurs by a combination of three basic heat transfer processes [19] conduction, convection and radiation. Each of these may be a complex function of component size, shape material and orientation [20].

Heat transfer is an energy-transport phenomenon, and conduction is the mode whereby energy is transported by molecular interchanges of kinetic energy. Conduction is therefore a microscopically phenomenon and can occur only when a physical medium is present [21]. In both thermal and electric conduction, which are frequently compared, the energy transport is accomplished by elastic collisions of adjacent molecules. In electric conduction the free–electron drift is an additional contribution to the conduction mode.

Heat transfer by conduction may also be treated macroscopically, and as suggested by Biot, but generally attributed to Fourier, heat flow is directly proportional to the temperature gradient and the cross-sectional area normal to the heat –flow path. Thus in one dimension:

$$q \propto -A\frac{dT}{dx} \qquad (1)$$

where q is the heat flow, A is the cross-sectional heat-flow path; T is the temperature, x is the distance, and dT/dx is the temperature gradient

The minus sign assures a positive heat flow in the presence of the negative temperature gradient required by the laws of thermodynamics; i.e., heat can not flow of its own accord from a lower to a higher temperature state. Insertion of proportionality constant yields the Fourier law:

$$q = -KA\frac{dT}{dx} \qquad (2)$$

where K is thermal conductivity coefficient in W/mk and A is a surface area in m^2

Convection is the transfer of sensible heat by fluid motion when the fluid moves over a surface that is at a different temperature. The mechanism for the fluid movement may naturally induce buoyancy forces resulting from a conduction temperature gradient, in which case the terms natural or free convection are used, or the fluid movement may be caused by some external force, such as a pressure difference or fan, in which case the term forced convection is applied. Although free-convection heat-transfer coefficients are low, many devices depend largely on this mode of heat transfer for cooling. In the electrical-engineering field, transmission lines, transformers, rectifiers, and electrically heated wires such as the filament of an incandescent lamp or the heating elements of an electric furnace are cooled by convection. As the temperature difference increases, the rate of heat flow also increases until a state of equilibrium is reached where the rate of heat generation is equal to the rate of heat dissipation.

Free convection is the dominant heat-flow mechanism from steam radiators, walls of a building, or the stationary human body in a quiescent atmosphere. The fluid velocities in free-convection currents especially those generated by gravity are generally low, but the characteristics of the flow in the vicinity of the heat-transfer surface are similar to those in forced convection. In free convection, as in forced convection, the flow may be laminar or turbulent, depending on the distance from the leading edge, the fluid properties, the body force,

and the temperature difference between the surface and fluid [22]

$$q = hA(T_1\text{-}T_2) \quad (3)$$

where q is the heat transfer (W), A is the surface area (m^2), T_1 and T_2 are the surface and field temperatures (K), respectively, and h is the convection coefficient ($W/m^2.K$)

All bodies emit electromagnetic radiation and the amount of radiation emitted by a body is primarily a function of its absolute temperature. In a vacuum, a body will reach a stable temperature when there is no net exchange of radiant energy between itself and its surrounding, i.e., when it emits energy at the same rate as it absorbs energy from its surroundings. If the body were to emit energy at a greater rate than that at which it absorbs energy then the temperature of the body would fall, and vice versa. The amount of radiation that is emitted by a flat surface determined by the Stefan-Boltzman physical law:

$$Q = \sigma \varepsilon_h A T^4 \quad (4)$$

where A is the area of the surface (m^2), T is the absolute temperature of the surface (K), ε_h is the hemispherical emissivity of the surface (the average all viewing directions, dimensionless), σ is the Stefan-Boltzmann constant (5.67×10^{-8} $W/m^2.K^4$). Where the heat exchange between two surfaces can be calculated usually in the form:

$$Q_{12} = \sigma A_1 \Phi_{12} (T_1^4\text{-}T_2^4) \quad (5)$$

Q_{12} is the net amount of energy leaving surface 1 which arrives at surface 2, A_1 is the area of surface 1, T_1 is the absolute temperature of surface 1, T_2 is the absolute temperature of surface 2, and Φ_{12} represents some combination of the surface emissivities together with a factor for the visibility of surface 1 from surface 2 (radiation shape factor) [23].

In natural convection a black or dark colored heat sink will perform 3% to 8% better than an aluminum heat sink in its natural silverfish color. This is due to the fact that dark colors radiate heat more efficiently [24]. Among the common plastics, the phenolic resin gives the highest yield of carbon during thermal pyrolysis, and they have been widely used as a surface charring ablative materials. Since a char is relatively weak, and is removed mechanically by high shear forces associated with the stream of gases during re-entry, fibers, silicon dioxide, refractory oxides, mineral asbestos, or even glass have been added to assist the char retention [25]. Sure carbon nanotubes are excellent one of there additives.

When fibers reinforced plastics (such as phenolic resin) are exposed to ablative environments, they first act as heat sinks. As heating progresses, the outer layer of polymer may become viscous and then begins to degrade, producing a foaming char. The char is a thermal insulation; the interior is cooled by volatile material percolatating through it from the decomposing polymer [26]. In phenolic resins, pyrolysis is found to occur by three general processes; (1) low temperature out gassing of free phenol present in the resin material; (2) formation of water from post-cure reaction at (423-673) K and, (3) thermal fragmentation of the polymer structure above 803K to yield lower molecular weight species, which are evolved, with hydrogen gas as the primary product (in the absence of oxygen) at 973K and above [27]. Phenolic compounds provide high char yield, low oxygen to minimize CO and CO_2 formation, and many carbon-hydrogen bonds, which provide the evolution of H_2 and CH_4 for transpiration cooling. The resin must also have good forming characteristics; good adherence to the fibers, and strength in the composite, and it must form a char that adheres well to the fiber reinforcements. During ablation, some pyrolytic deposition of carbon from the CH_4 or other gases in the outer portions of the char can contribute to the strength and resistance to mechanical removal from the flow field [28]. The ablation rate for ablative materials was calculated by dividing the original thickness of the specimen by the time to burn through as follows [29]:

$$A_r = d_s / b_t \quad (6)$$

where A_r is the ablation rate (m/s), d_s is thickness of specimen (m) and b_t is the burn through time (s)

The theoretical simulation of ablative test of a thermal insulator is considered as an important process since it reduces many efforts, time and raw materials that are used in trail and error of the experimental procedure. This simulation is performed by using the values of thermal parameters of the specific material. In this study a simulation of the ablation of three-dimensional a square insulator according to ASTM E285-80 standards is performed. The thermal properties of the insulator are known. This insulator is subjected to an oxyacetylene flame of (2773-3273) K. The simulation also supposes a certain temperature at which the insulator is removed by gravity or the mechanical effect of the flame [30].

3. Simulation Approach

Partial differential equations are encountered in many branches of physics and engineering in which more than one dimension exist in the differential equations. Heat transfer, diffusion, mechanical, electrical, magnetic and even Schrödinger equations are examples of partial differential equations. These equations transform to ordinary differential equations when they become one-dimensional only.

Numerical solutions of partial differential equations are an important class of solutions since

many of the equations cannot be solved analytically. Many such numerical methods were invented such as finite difference method (FDM), finite element method (FEM), boundary value method… etc [31]. The simplest of these methods is FDM. The widest in use and more sophisticated is the FEM. Scientists prefer FDM since basic scientific experiments does not contain difficult geometries, which is not the case for engineers. Engineers prefer FEM since geometry is usually an important issue in engineering practice.

Dividing a component into rectangular elements (curved surfaces are therefore approximated as stepped surfaces). Each element is then assumed to be at a uniform temperature and the heat transfer between each pair of adjacent elements can be determined as a function of the element size, shape, properties and temperature. The large numbers of equations that result from this definition process are then solved automatically to determine the steady-state temperature distribution and the net heat transfer.

Finite difference method relays on using difference approximations to be substituted in the partial differential equations. For example, first derivative of a function $f(x)$ can be approximated by [31]:

$$f'(x) = \lim_{h \to 0} \frac{f(x+h) - f(x)}{h} \qquad (7)$$

While second derivative is given by

$$f''(x) = \lim_{h \to 0} \frac{f(x+h) + f(x-h) - 2f(x)}{h^2} \qquad (8)$$

Heat transfer equation in Cartesian coordinate is given by

$$\frac{\partial T}{\partial t} = \frac{K}{\rho c}\left(\frac{\partial^2 T}{\partial x^2} + \frac{\partial^2 T}{\partial y^2} + \frac{\partial^2 T}{\partial z^2}\right) + \dot{Q} \qquad (9)$$

where x, y and z are the rectangular coordinates, K is the thermal conductivity coefficient, ρ is the density, c is the specific heat, T is the temperature, t is the time, and Q is the latent heat of phase transformation Heat can be also transferred by convection or radiation that occurs generally at the boundary of the simulated piece.

4. Experimental Approach

The experimental work is divided in to three parts. The first part includes specimens preparation, using Hot-press technique. The second part includes two empirical tests. The first set of tests includes the thermal conductivity coefficient measurement using Lee's disc method, and the second set of tests includes ablative test using flame technique. The third part includes a computer simulation for ablative test using finite difference method. A commonly used method for preparing nanotube-ceramic/polymer nanocomposites has involved with mixing nanotube - ceramic dispersions with solution of the polymer and then evaporating the solvent in a controlled way. Phenol-formaldehyde resin material (Resole type) designated by (PFR) in form of liquid was used as (matrix) in preparation of nanocomposite materials. Resole in form of liquid was dried in an electric oven at (323K) for three hours to obtain the resole in form of solid, followed by milling to a desirable size suitable for molding operation. Resole, which was prepared by this method, was used to prepare a reference specimens according to different types of testing standard requirement. Resole in form of liquid was solved using ethanol to obtain a suitable matrix. Then porcelain with constant volume fraction (20 vol.%) was dispersed as well as SWCNTs (1%, 2%, 3%, and 4%) vol.% in matrix respectively, which was prepared as above, followed by drying the mixture in air using dispersion method on a dry plate for three hours. The mixture was pre- cured using an oven at (353K) for three hours.

Porcelain-SWCNTs/resole mixture in form of liquid was dried in an oven at (323K) for three hours to obtain the mixture in form of solid, followed by milling to a desirable size, suitable for mixing operation. The addition, which was used porcelain powder filler, was dried by using an oven at (473K) for three hours to reduce humidity. Hot–press technique was used in this work to prepare the nanocomposites specimens of resole matrix, using flash mold.

Simulation program of heat transfer in three dimensions of ablative test for four groups of SWCNTs – porcelain / resole nanocomposites were carried out using finite difference method. The program was written in FORTRAN-90 language using a computer type Pentum-4. The program was starting to solve heat conduction equation in three dimensions.

5. Results And Discussion

Figure (1) shows the comparison of the influence of CNTs vol.% on the ablation rate of porcelain/resole matrix of simulation operation with the experimental results of oxy-acetylene torch. It can be seen from the figure that, the ablation rate was decreased when volume fraction increased, but with different percentages for experimental and simulation results. It can be seen from this figure that the ablation rate of experimental value was lower than simulation values because of experimental error, and as well as the interface effect between the matrix and the carbon nanotubes, also the high adhesion between them.

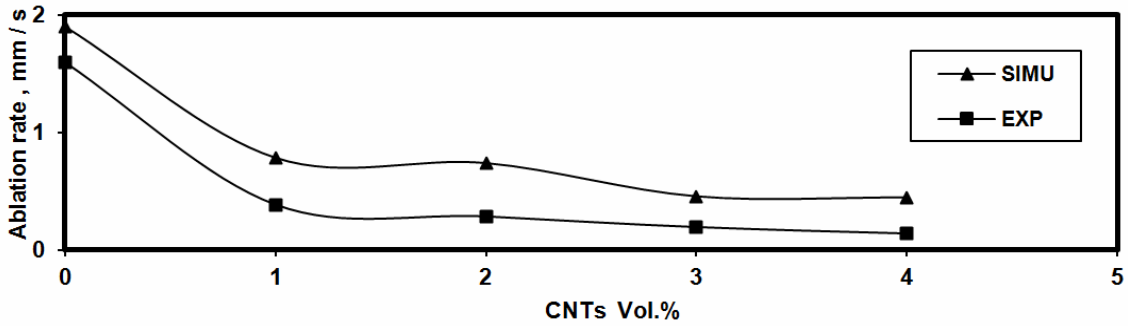

Fig. (1) Comparison of CNTs vol.% on the ablation rate of (porcelain/resole) by simulation operation with the experimental results of oxy-acetylene torch temperature

Figure (2) shows temperature distribution after 44.57s when the matrix (porcelain/resole) is punctured by simulation operation of oxy-acetylene torch. From the Figure, it can be seen three temperature distribution regions, and a series of numbers which indicate the temperature distribution values of the last two nodes of specimen.

Figures (3) and (4) show the temperature distribution after different burn through time when (1, and 4) CNTs vol.% of (porcelain/resole) matrix is punctured by simulation operation of oxy-acetylene torch. It can be seen from this Figures that the thermal insulation of the material, how enhancement when the CNTs vol.% is added to the matrix, where the temperature distribution values of the last nodes of specimens were decreased, specially, near the punctured region.

Ablation phenomena can be explained by using ablation mechanism; when a thermal flux was applied on the surface of nanocomposite material, they first act as heat sinks: as heating progresses, the outer layer of polymer may become viscous and then begins to degrade, producing a foaming char. The char is a thermal insulation; the interior is cooled by volatile material percolating through the decomposing polymer. During percolation, the volatile materials are heated to very high temperatures with decomposition to low molecular weight species, which are injected into the boundary layer of gases. This mass injection creates a blocking action which reduces the heat transfer to the material. Thus, a char-forming resin acts as a self-regulating ablation radiator, providing thermal protection through transpiration cooling and insulation.

Ablation of the char occurs by sublimation of carbon nanotubes and oxidation in the boundary layer with concomitant vaporization. The rate of ablation slows as the rate of char surface recession equals or exceeds the recession rate of the interface between the char and virgin matrix. Since this part provides the essential gas for transpiration cooling of the char, the decomposition products are important. With the continuous thermal decomposition reactions, the pyrolysis gases were produced and exceeded inside the constitute char structure, which was characterized with low porosity and permittivity.

With the rising of temperature, the thermal decomposition operation was continued; with continuous production of these gases, which lead to raise the internal pressure. This, internal pressure was continued with increment of temperature till reaching the maximum value. At that, thermo-chemical expansion will take place, causing the increment of porosity and permittivity of the composite material. By that, the exceed gases could pass through the composite material, and in general, this current of flow gases was associated high shear forces, causing removal of carbonaceous char, so, the progress gases in carbonize zone direction, will be worked to inhalation the thermal energy, which is reached the pyrolyzed zone, because of transferring of heat by convection. If the pyrolysis and thermal expansion reactions were continued, the porosity and permittivity well would be increased, and that lead to increment of flow rate of gases and decrease of internal pressure. At that, sudden high shrinkage well be taken to the material, which is returned to the fact, that the elastic recovery was taken.

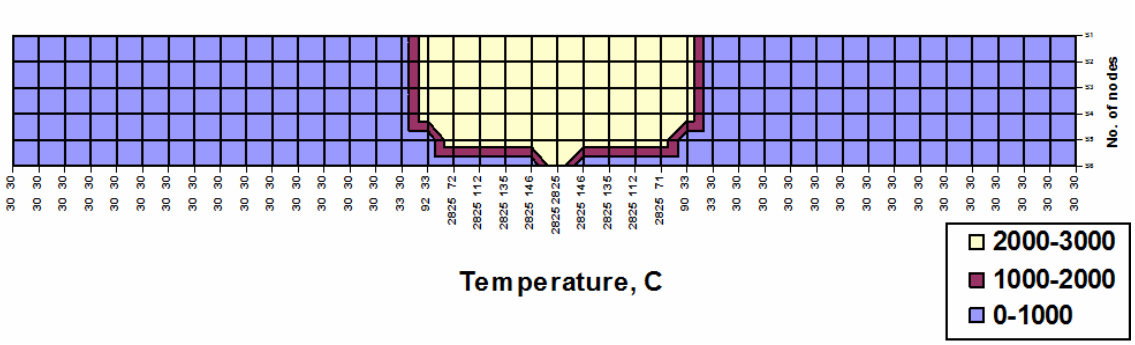

Fig. (2) Temperature distribution after 26.88 seconds when porcelain/resole is punctured by simulation operation of oxy-acetylene torch temperature

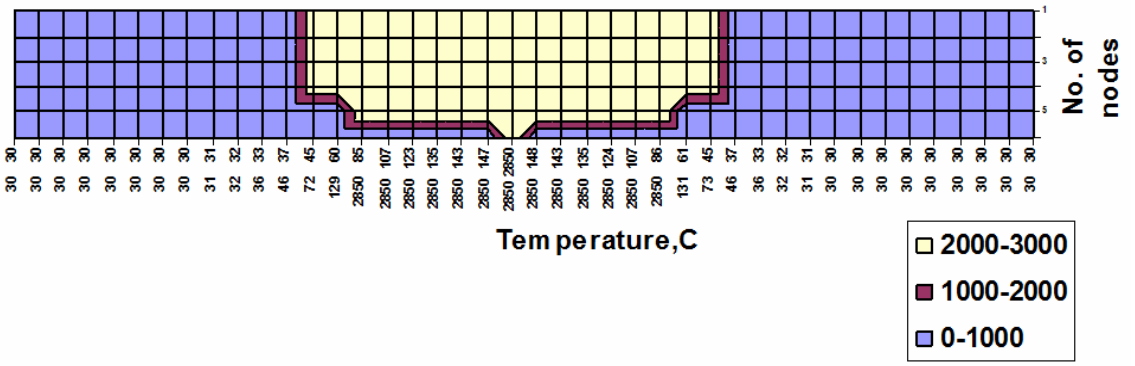

Fig. (3) Temperature distribution after 88.32 seconds when 1 CNTs vol.% porcelain/resole is punctured by simulation operation of oxy-acetylene torch temperature

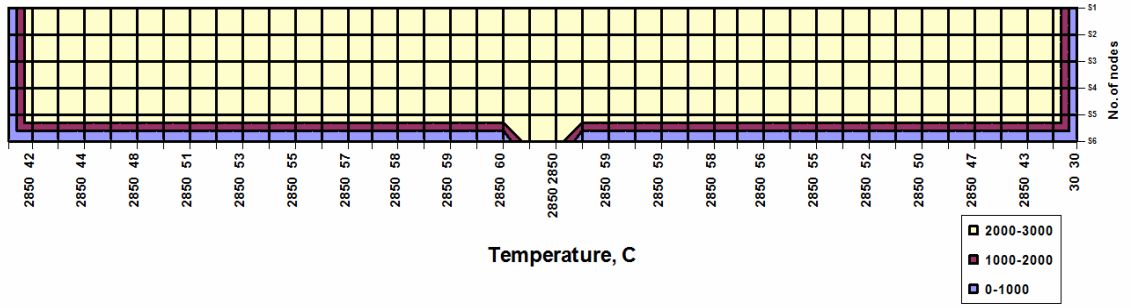

Fig. (4) Temperature distribution after 220.12 seconds when 4 CNTs vol.% porcelain/resole is punctured by simulation operation of oxy-acetylene torch temperature

6. Conclusions

From this study, the following remarkable points can be concluded. Reinforcing of porcelain/resole matrix by CNTs, has improved the thermal and ablation characteristics of nanocomposites in different volume fraction, depending on kind of additives, characteristic of its properties, and nature of interface between the matrix and reinforcement additives. There is a high influence of CNTs (direction, distribution), with respect to thermal flux, on thermal conductivity values. The produced nanocomposites have high ablation resistance at temperature exceed 2773K; because an earlier char operation has been taken place. Results of thermal transfer indicted that the increment of thermal conductivity and decrement of ablation rate lead to better thermal distribution, which leads to increment of thermal insulation efficiency for composites.

References

[1] K.I. Winey and R.A. Vaia, *MRS Bull.*, 32 April 2007.
[2] Y. Fukushima and S. Inagaki, *J. Inclusion Phenom.*, 5 (1987) 473.
[3] Y. Fukushima et al., *Clays Clay Miner.,* 23 (1988) 27.
[4] A. Usuki et al., *J. Mater. Res.,* 8 (1993) 1174.
[5] Y. Kojima et al., J. Mater. Res. 8, 1185 (1993).
[6] R.A. Vaia, H. Ishii and E.P. Giannelis, *Chem. Mater.,* 5 (1993) 1694.
[7] T.P. Lan and T.J. Pinnavaia, *Chem. Mater.,* 6 (1994) 2216.

[8] R.A. Vaia and E.P. Giannelis, *MRS Bull.,* 26 (2001) 394.
[9] R.A. Vaia and H.D. Wagner, *Mater. Today,* 7 (2004) 32.
[10] A. Bansal et al., *Nature Mater.,* 4 (2005) 693.
[11] R. Krishnamoorti, R.A. Vaia and E.P. Giannelis, *Chem. Mater.,* 9 (1996) 1728.
[12] F.W. Starr, T.B. Schroeder and S.C. Glotzer, Macromolecules 35 (2002) 4481.
[13] W.D. Callister, **"Materials Science and Engineering: An Introduction"**, John-Wiley & Sons, Inc. (NY), (2000) 2, 40, 193, 475.
[14] D.R. Askeland, **"The Science and Engineering of Materials"**, van Nostrand Reinhold Int. Co. Ltd (Hong Kong) (1988).
[15] E. Bauer and H. Dietze, *IEEE Trans. on Electric. Insul.*, 16(3) (1981) 209–219.
[16] G. Lubin, **"Handbook of Advanced Plastics Composites"**, Litton Educational Co. (NY), (1969).
[17] A. Knop and W. Scheib, **"Chemistry and Application of Phenolic Resin"**, Springer-Verlag (NY), (1979) p125.
[18] R. Dendy, **"Plasma Physics: an Introduction Course"**, Cambridge University Press (Oxford) (1996).
[19] M. Kutz, **"Mechanical Engineer's Handbook",** John-Wiley & Sons Inc. (1986) p.20.
[20] F. Kreith, **"Principles of heat transfer"**, *3rd* ed., In-text Educational Publishers (1973).
[21] E. Schmid, G. Spitz and W. Losch, **"Theoretical Physics on the personal computer"**, Springer-Verlag (1989).
[22] J.P. Hallman, **"Heat Transfer"**, McGraw-Hill (NY) (1982).
[23] A. Bejan, **"Heat Transfer"**, John-Wiley & Sons (UK) (1993).
[24] G.T. Murray, **"Introduction to Engineering Materials"**, Marcel Dekker (NY) (1993) p.25.
[25] M. Ohring, **"Engineering Materials Science"**, Academic Press (San Diego) (1995) p.52.
[26] K.M. Ralls, T.H. Courtney and J. Wulff, **"Introduction to Materials Science and Engineering"**, John-Wiley & Sons (NY) (1976).
[27] W.F. Smith, **"Principles of Materials Science and Engineering"**, 3rd ed., McGraw-Hill Book Co. (NY) (1995) p.6.
[28] L.H. van Vlack, **"Elements of Materials Science and Engineering"**, 6th ed., Addison-Wesley Publishing Co. (1989).
[29] M.A. Meyers and K.K. Chawla, **"Mechanical Behavior of Materials"**, Prentice-Hall (NJ) (1999) p.31.
[30] M. Rappaz, *Int. Mater. Rev.*, 34(3) (1989) 131.

This article was reviewed at NANOTECH Laboratories, NICHE, Tamilnadu, INDIA, School of Applied Sciences, University of Technology, Baghdad, IRAQ, and Department of Physics, College of Education, The Iraqi University, Baghdad, IRAQ

NEW SCIENTIFIC INDEXED PERIODIC JOURNAL

Printed in Iraq

Journal of Educational and Scientific Studies

(JESS)

ISSN 2224 – 8048

Sponsored and Published by

College of Education, The Iraqi University, Baghdad, Iraq

P. O. Box 55441, Baghdad 12001, Iraq

The *Journal of Educational and Scientific Studies (JESS)* is a peer reviewed journal of high quality devoted to the publication of original research papers from educational, theoretical and applied sciences and their broad range of applications. JESS publishes quality original research papers, comprehensive review articles, survey articles, book reviews, dissertation abstracts in education and science as well as their applications in the broadest sense. It is intended that the journal may act as an interdisciplinary forum for educational and scientific societies. Innovative applications and material that brings together diverse areas of education and science are particularly welcome. Review articles in selected areas are published from time to time. It aims to disseminate knowledge; provide a learned reference in the field; and establish channels of communication between academic and research experts, policy makers and executives in industry, commerce and investment institutions. JESS is a quarterly specialized periodical dedicated to publishing original papers, letters and reviews in educational and scientific studies.

Majed A. Salman
Sergey G. Zhirov
Anatoly A. Koptelov

Federal Center of Dual-Use Technologies "Soyuz" ul. Academician Zhukova 42, Moscow, RUSSIA

Analytical Calculation of Heat Conduction in Two-Phase Heterogeneous Materials

The method of the calculation of the heat conduction of the two-phase heterogeneous materials, where the filler's participles of the cubic form by the at random fashion distributed in the matrix's volume is considered. The given method of the effective heat conduction of the heterogeneous materials is based on the probability principles of the analysis of their structure. Such approach allows not only predict the average magnitudes of the heat conduction of the binary or many-component compositions but also to determine the bounds where their measured valuations will be realized with the given of the degree of certainty. The received formulas are applied in a wide range volume correlation changes and heat conduction of the separated components and also typical sizes of the researched samples.

Keywords Heat conduction, Heterogeneous materials, Probability, Two -phase Analysis
Received: 24 March 8/2011, **Revised**: 22 August 2011, **Accepted:** 29 August 2011

1. Introduction

Heterogeneous propellant combustion is a very complicated process. The complexity starts with the material itself. Composite propellants are a mix of crystalline oxidizer and polymer binder, and have heterogeneous length scales on the order of 100 μm or more. When these materials are burned, flames with characteristics of both premixed flames and diffusion flames can form in the gas phase [1-5]. The surface of the burning propellant is multi-phase and three-dimensional, resembling a boulder field on which molten binder can flow. It is important to realize that significant chemistry is occurring in the gas phase, in the solid phase, and at the surface. When materials such as aluminum are added to the mix, the complexity increases by another order of magnitude. It is safe to say that all models previously developed or currently in development account for only a fraction of these phenomena [6-10].

The ability to accurately measure the thermal conductivity of insulation materials is critical to the establishment, assurance and enforcement of thermal performance standards. There is little point in devising parameters for quality assurance if compliance by quantitative measurement cannot be established. Thermal conductivity apparatuses are notorious for systematic errors and their performance should be verified over the intended temperature range of measurement on appropriate 'standard' materials [11-15]. The experimental design for all the thermal conductivity values presented in the literature have been based on the assumption the Fourier equation for heat conduction in a solid is valid. Unfortunately this experimental design is flawed because it neglects the effect of the temperature dependence of the thermal conductivity. Neglecting the temperature dependence of the thermal parameters introduces systematic errors into, for example, the estimated thermal conductivity values. These systematic errors are typically of the order of 5% to 20% in typical heat flow in buildings experiments. In recent years these systematic effects have become large when compared to the experimental uncertainties. Obviously such systematic effects will effect and undermine the currently adopted national and international standards. It is shown in this project that acceptably accurate information can be achieved by improving the measurement and analysis procedures that are used to determine the thermal properties of solid materials [16-20].

Thermal conduction measurement techniques rely on the direct measurement of the heat that passes through the material and the temperature at different positions in the material. The techniques also require thermometers to measure the temperature and its derivatives in the material as they change with time. A number of steps were taken in this project to ensure that the data collected were of high quality. The temperature dependence of the electrical resistance signal cables was reduced by employing compensation cables and the thermal stability of these cables was improved by surrounding them with several layers of Aluminised Mylar. Faraday cages were used to minimise the influence of external factors on the signals. Earth loop and mains noise were largely eliminated where possible by using battery power for the electronics, logging equipment and signal amplifiers and 1000Ω Platinum resistance thermometers were used in preference to the usual 100Ω thermometers. A temperature difference sensor has been developed by RAL during the project with an appropriate calibration apparatus that has a repeatable precision of better than 0.200 mK. In order to get the best

accuracy when installing the thermometer in an experiment, it is essential that the calibration be made in conditions as close as possible to those go like it to be experienced by the sensors. The experimental design of the prototype has ensured that the uncertainty in the variables such as linear dimension, positioning of sensors and the error due to the radial loss of heat flux are all much less than 1%. The dominant source of uncertainty is in the measurement of the power entering the radiation cavity at the top of the bar or the measured heat flux that propagates along the bar. The apparatus has been designed such that they heat flux of 1W m^{-2} will result in a temperature difference of 1 mK [21-25].

2. Analysis and Treatment

Let's consider a binary system with constant values of the heat conduction of the components λ_1 (matrix) и λ_2 (filler). We usually get the design equations for heat conduction λ of the composition systems by dividing material with the help of the adiabatic or isothermic surfaces [1]. Let's denote the received comparative valuations of the effective heat conduction compositions γ' and γ'' (γ', $\gamma'' = \lambda_{eff}/\lambda_1$) respectively. The calculated values for γ' and γ'' go with experimental data if the filler directed in the matrix length and breadth of direction distribution heat. It's better to find the effective heat conduction in the form of linear aggregate γ' and γ'' for the systems with chaotic disposition of the participles filler:

$$\gamma_{eff} \equiv \frac{\lambda_{eff}}{\lambda_1} = A\gamma' + B\gamma'' \qquad (1)$$

where A and B the numbers, satisfying the proportion A + B = 1.

The coefficients A and B characterize isotherms distortion near participles of the filler. They usually suppose in deriving design formula, that lines of flow (of the heat flow) are parallel. However, particularly, if $\lambda_2/\lambda_1 \equiv \nu \to \infty$ almost all lines of flow pass through the filler. In this case the ratio of the lines of flow by the considering cross-sectional to the general numbers of the lines, passing through the surface, which is perpendicular to the heat flow with the same its density, equals volumetric degree of the P filler. In case that $\nu = 0$, this proportion equals 1 – P. If $0 < \nu < \infty$ the distortion of the lines of flow determine not only by the filler degree but also by the thermal and physical characteristics of the material of the filler and the matrix, character of the heat exchange on their bounds and etc. If we consider these factors, it'll result in complication of the considering problem. So then we'll adopt the assumption that with all $\nu > 1$ in the formula (1) B = P, A = 1 – P, and with all $\nu < 1$ B = 1 – P, A = P. Here we, of course, narrow, in some cases, the bounds of the got below formulas [16-18].

Let's write the proportion for the effective heat conduction λ or the heterogeneity element by emphasizing the heterogeneity element with adiabatic surfaces:

$$\frac{\delta+\beta}{\lambda} = \frac{\delta}{\lambda_1} + \frac{\beta}{\lambda_2} \qquad (2)$$

where by putting signs $\lambda / \lambda_1 \equiv \gamma$, we'll get:

$$\gamma = \frac{\delta+\beta}{\delta+\frac{\beta}{\nu}} \qquad (3)$$

Let's use the above got formula for the joint density to find density of distribution of the chance function γ:

$$f(\beta,\delta) = \frac{\ln P \cdot \ln(1-P)}{\alpha P} \cdot \frac{1}{\beta} P^{\beta/\alpha}(1-P)^{\delta/\beta} \qquad (4)$$

The distribution function of the comparative heat conduction γ, the proportion will be determined:

$$F(\gamma) = \int_0^{\infty}\left[\int_a^b f(\beta,\delta)d\delta\right]d\beta \qquad (5)$$

Here we have the limit of integration a and b, which we can determine from the proportion (3), depending on ν the different values are adopted:

if $\nu<1$ a=0, $b = \frac{\beta}{\nu}\cdot\frac{\gamma-\nu}{1-\gamma}$;

if $\nu>1$ $a = \frac{\beta}{\nu}\cdot\frac{\nu-\gamma}{\gamma-1}$, b=+∞

If we integrate we'll get:

$$F(\gamma) = 1-(1-P)^{\frac{1}{\nu}\cdot\frac{\gamma-\nu}{1-\gamma}} \qquad (\nu < 1) \quad (6)$$

$$F(\gamma) = (1-P)^{\frac{1}{\nu}\cdot\frac{\gamma-\nu}{1-\gamma}} \qquad (\nu>1) \quad (7)$$

The differentiation of the (6) and (7) result in density distribution expressions $f(\gamma)$, and differ only by multipliers: 1 - ν if $\nu < 1$ and ν - 1 if $\nu > 1$. If we combine these expressions into one, we'll the following density distribution γ:

$$f_1(\gamma) = -\frac{|\nu-1|}{\nu}\cdot\frac{\ln(1-P)}{(1-\gamma)^2}\cdot(1-P)^{\frac{1}{\nu}\cdot\frac{\gamma-\nu}{1-\gamma}} \qquad (8)$$

The central tendency of the comparative heat conduction γ' will determine by the proportions:

$$\gamma' = m_\gamma = \int_1^{\nu}\gamma f(\gamma)d\gamma \qquad (\nu>1) \qquad (9)$$

$$\gamma' = m_\gamma = \int_{\nu}^{1}\gamma f(\gamma)d\gamma \qquad (\nu < 1) \qquad (10)$$

If we integrate (9) and (10), we'll get formula for γ', true for any ν:

$$\gamma' = 1-\frac{1-\nu}{\nu}\left((1-P)^{-\frac{1}{\nu}}\ln(1-P)\cdot Ei\left[\frac{\ln(1-P)}{\nu}\right]\right) \qquad (11)$$

where

$$Ei(x)=\int_{-\infty}^{x}\frac{e^t}{t}dt$$

is an integral exponent

We should cut the material with the surface to find γ'', which is perpendicular to the heat flow and isolate in this surface an area S in n times larger of the sectional area of the one participle of the filler ($S = n\alpha^2$). The possibility that cross-sectional S hits exactly m participles of the filler equals:

$$F_m = C_n^m P^m (1-P)^{n-m} \qquad (12)$$

The possibility that all square will be filled with filler (m = n) equals P^m. If we continue to reason further as we did in our work [2], we'll get the similar expression by the structure for density of distribution of the squares S_2, filled with filler phase to get the expression for density of distribution of the length continuous phase filler:

$$f(S_2) = -\frac{\ln P}{\alpha^2} P^{S_2/\alpha^2} \qquad (13)$$

We find in the same way density of distribution of the squares S_2, filled with matrix material:

$$f((S_1) = -\frac{\ln(1-P)}{\alpha^2}(1-P)^{S_1/\alpha^2} \qquad (14)$$

If we isolate the layer with the thickness Δx in the material, which is set between two isothermic surfaces, we'll get the following expression for effective heat conduction λ determination:

$$\lambda\frac{\Delta T}{\Delta x}S = \lambda_1\frac{\Delta T}{\Delta x}S_1 + \lambda_2\frac{\Delta T}{\Delta x}S_2 \qquad (15)$$

where ΔT is temperature difference in the selected layer.

Then if we put the symbols

$$q = \frac{S_2}{S_1}$$

and considering, that $S_1+S_2=S$, we'll get the following expression for relative heat conduction of the heterogeneity element by dividing material with the help of isothermic surfaces:

$$\gamma = 1-(1-\nu)\frac{q}{1+q} = \varphi(q) \qquad (16)$$

where

$$q = \frac{\gamma-1}{\nu-\gamma} = \psi(\gamma) \qquad (17)$$

Let's first find distribution function F(q):

$$F(q) = \int_0^{\infty} f(S_1)\left[\int_0^{qS_1} f(S_2)dS_2\right]dS_1 \qquad (18)$$

We'll get by putting (18) into expressions (13) and (14):

$$F(q) = 1 - \frac{\ln(1-P)}{\ln(1-P)+q\cdot\ln P} \qquad (19)$$

We'll find density of distribution f(q) by differentiate:

$$f(q) = \frac{\ln(1-P)\cdot\ln P}{[\ln(1-P)+q\cdot\ln P]^2} \qquad (20)$$

As consistent with [3]:

$$f(\gamma) = \varphi[\psi(\gamma)]\cdot|\psi'(\gamma)|$$

We can find density of distribution considering (16) and (17):

$$f_2(\gamma) = \frac{|\nu-1|\Phi(P)}{\{\nu-\Phi(P)+\gamma[\Phi(P)-1]\}^2} \qquad (21)$$

where

$$\Phi(P) = \frac{\ln P}{\ln(1-P)}$$

We can determine the central tendency of the relative heat conduction γ'' by the formulas similar to (9) and (10). We'll get by integrating:

$$\gamma'' = \frac{\nu-\Phi(P)}{1-\Phi(P)} + \frac{(\nu-1)\Phi(P)}{[1-\Phi(P)]^2}\ln\Phi(P) \qquad (22)$$

Considering the proportions (11) and (22) and also the above made assumption concerning coefficients A and B in the formula (1), we can write the final expression for central tendency of the heat conduction of the heterogeneous material; specifically if $\nu > 1$:

$$\gamma_{eff} = (1-P)\cdot\left\{1-\frac{1-\nu}{\nu}\left((1-P)^{-\frac{1}{\nu}}\ln(1-P)\cdot Ei\left[\frac{\ln(1-P)}{\nu}\right]\right\}+P\cdot\left\{\frac{\nu-\Phi(P)}{1-\Phi(P)}+\frac{(\nu-1)\Phi(P)}{[1-\Phi(P)]^2}\ln\Phi(P)\right\} \qquad (23)$$

With the made assumptions, the effective heat conduction doesn't depend on the participle size in the filler. The dependence γ_{eff} from P with different ν is shown in the Fig. (1).

The estimated value of the difference meanings of the heat conduction of the samples is a great interest of practical applications. We'll get the following expression for density of distribution of the relative heat conduction with the use material dividing circuit by adiabatic surfaces if we summarize the used binominal distribution in case of arbitrary parameter $n = L/\alpha$ (where L is sample's thickness towards heat flow) in the work [2].

$$\varphi(\gamma) = \frac{\nu\Gamma(n+1)P^{Cn}(1-P)^{n(1-C)}}{\gamma^2(\nu-1)\Gamma(Cn+1)\Gamma(n-Cn+1)} \qquad (24)$$

where

$$C = \frac{\nu(\gamma-1)}{\gamma(\nu-1)}$$

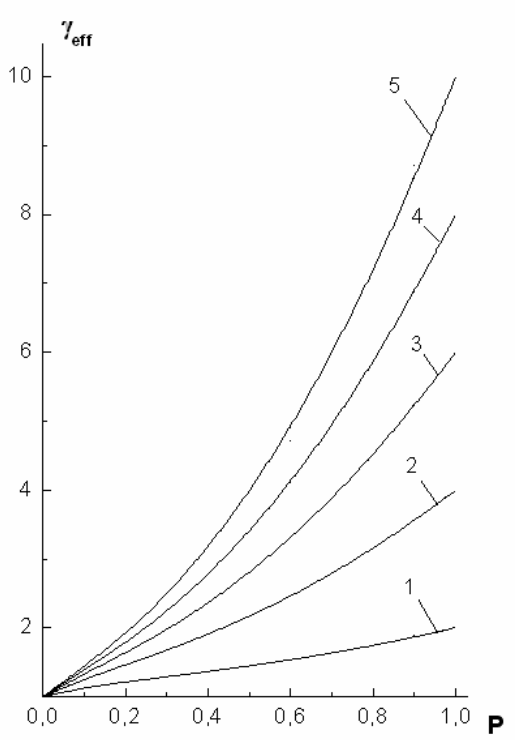

Fig. (1) The dependence of the relative effective heat conduction from the volumetric degree of the filling, calculated by formula (23) with heat conduction proportions of the filler and matrix ν = 2 (*1*), 4 (*2*), 6 (*3*), 8 (*4*) и 10 (*5*)

The dependences with φ(γ) different n for the case P = 0,3 and ν = 5 are shown in the Fig. (2). If we know φ(γ), the possibilities of getting heat conduction valuations, lying inside of the fixed bounds will be easy to calculate.

The dependence form parameter k of the possibility V of the receiving relative heat conduction valuations, which is differing from average of distribution (γ_0) to the value not more ± kγ_0:

$$V = \int_{\gamma_0(1-k)}^{\gamma_0(1+k)} \varphi(\gamma)d\gamma \qquad (25)$$

The calculation by the formula (25) is made for P=0.7 and different n and ν. As it was expected, the value V is strongly decreasing with the physical heterogeneity material increase (ν) and material thickness decrease (L), as in Fig. (3).

Conclusion

It's enough to calculate the effective heat conduction of the one heterogeneity element to find the effective heat conduction composition. Let as in [2], δ is a continuous length phase of the matrix, β is a length phase of the filler, z = δ + β is an element's length of the heterogeneity. The filler consists of the cubes with the size of the edge α, the bounds of which are reciprocally parallel; the heat flow is directed perpendicular to one of the bounds.

The received dependences allow us to find the limits, where heat conduction of the heterogeneous two-phase materials can vary depend upon sample's thickness, filler degree and heat conduction components.

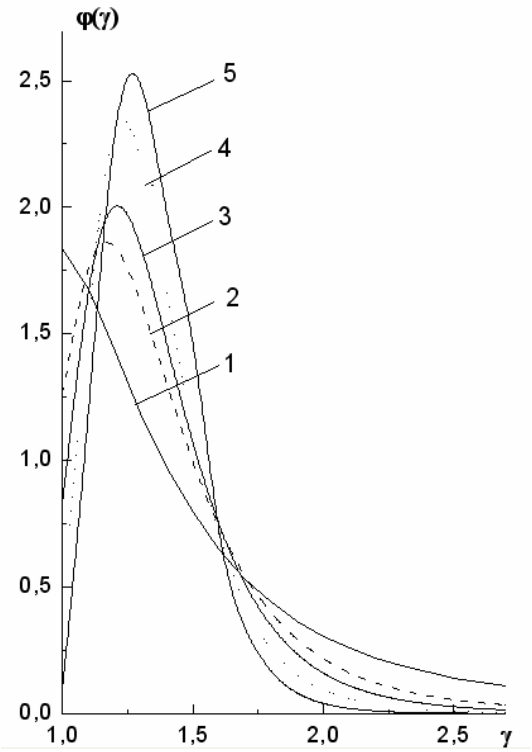

Fig. (2) The density of distribution of the relative heat conduction, calculated by formula (24) if proportion valuations of the sample's thickness to the size of the participle filler n = 2 (*1*), 5 (*2*), 7 (*3*), 10 (*4*) и 15 (*5*)

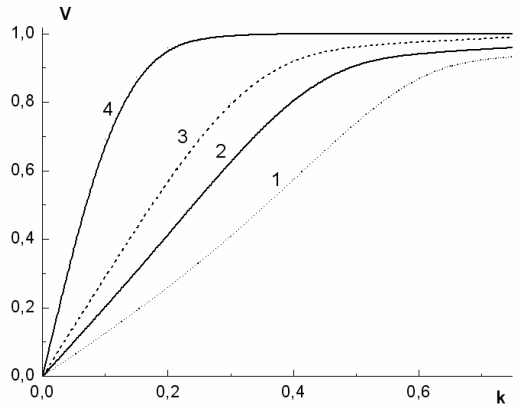

Fig. (3) The possibility of the getting valuations of the relative heat conduction, which is differing from the average of distribution (γ_0) to the value not more ± kγ_0 with P = 0,7 and different n and ν:
1 - n = 5.75, ν = 10; 2 - n = 23, ν = 100; 3 - n = 23, ν = 10; 4 - n = 230, ν = 10

References

[1] G.N. Dulnev and Y.P. Zarichnyk, "The heat conduction of the compositions and composite materials", St. Petersburg.: Energiy, 1974.

[2] S.G. Zhirov and A.A. Koptelov, "The mathematical model of heterogeneous materials structure with interpenetrating components", The report for the VII International seminar. Ekaterinburg, 2004.
[3] E.S. Ventcel, "The Probability Theory", Moscow.: Nauka, 1969.
[4] V.E. Alemasov et al., **"Thermodynamic and Thermophysical Properties of Combustion Products",** Vol. 1. Computation Methods. Moscow: VINITI (1971).
[5] H. Arisawa and T.B. Brill, *Combustion and Flame*, 106 (1996) 131-143.
[6] H. Arisawa and T.B. Brill, *Combustion and Flame*, 106 (1996) 144-154.
[7] A.I. Atwood et al., *J. Propulsion and Power*, 15(6) (1999) 748-752.
[8] J.D. Baum and J.N. Levine, *AIAA J.*, 20(7) (1982) 955-961.
[9] W.H. Beck, *Combustion and Flame*, 70 (1987) 171-190.
[10] M. Beckstead, R. Derr and C. Price, *AIAA J.*, 8(12) (1970) 2200-2207.
[11] M. Beckstead and J. Hightower, *AIAA J.*, 5(10) (1967) 33-42.
[12] C. Beiter and E. Price, *J. of Propulsion and Power*, 14(2) (1998) 160-165.
[13] T.L. Boggs, *AIAA J.*, 8(5) (1970) 867-873.
[14] C. Bowman et al. "GRI-Mechanism,1996, http://www.me.berkeley.edu/gri-mech/"
[15] M.Q. Brewster, "**Thermal Radiative Transfer and Properties**", John-Wiley & Sons (1992).
[16] T.B. Brill, *J. of Propulsion and Power*, 11(4) (1995) 740-751.
[17] T.S. Brill, "Surface Chemistry of Energetic Materials at High Temperatures," *Mat. Res. Soc. Symp. Proc.*, 296(1993) 269-280.
[18] K.P. Brooks and M.W. Beckstead, *J. of Propulsion and Power*, 11(4) (1995) 768-780.
[19] J. Buckmaster, T. Jackson and J. Yao, *Combustion and Flame*, 117 (1999) 541-552.
[20] R. Cantrell, F. McClure and R. Hart, *AIAA J.*, 3(3) (1965) 418-426.
[21] L. Caveny, T. Ohlemiller and M. Summerfield, *AIAA J.*, 13(2) (1975) 202-205.
[22] Chemistry Web Book, http://webbook.nist.gov, 2000
[23] H. Cheung and N.S. Cohen, *AIAA J.*, 3(2) (1965) 250-257.
[24] P. Clavin and D. Lazimi, *Combus. Sci. Technol.*, 83 (1992) 1-32.
[25] R. Coates and S. Kwak, *J. Spacecraft*, 9(1) (1972) 742-745.

Introduction to Autonomous Mobile Robots

By
Roland Siegwart
Illah R. Nourbakhsh

Contents
Acknowledgments xi
Preface xiii

Novel Optical Fiber Sensor Based on SGMS Fiber Structure for Measuring Refractive Index of Liquids and Gases

Jassim K. Hmood

Department of Laser and Optoelectronics Engineering, University of Technology, Baghdad, IRAQ

In this paper a single mode-gap-multimode-single mode fiber structure (SGMS) as refractive index sensor is demonstrated. A beam propagation method (BPM) for the circular symmetry waveguide is employed for numerical simulations of the light propagation performance in such fiber devices. The multimode interference effect is revealed to design optical fiber sensor with reasonable linearity in wide range of refractive indices. A simple way to predict and analyze the spectral response of the SGMS structure is presented with the derived approximated formulations. The proposed sensor is realized by using standard optical fibers.

Results indicate that the proposed SGMS structure can be exploited for measuring a broad refractive index range with reasonable high resolution. The results achieved for refractive indices in the range of 1.1 to 1.43 have best linearity with correlation coefficient 0.9991 at wavelength of 1550 nm. Therefore, it can be suggested that the SGMS structure fibers are attractive for measuring refractive index of both gases and aqueous solutions such as chemical liquids, biological, and biochemical sensing.

***Keywords*:** Optical fiber sensor, Multimode interference, Refractive index, Self-imaging
Received: 19 September 2011, **Revised**: 27 October 2011, **Accepted**: 3 November 2011

1. Introduction

Optical fiber based refractive index (RI) sensors have attracted considerable interest in recent years, because of their many excellent characteristics, including corrosion resistance, immunity to electromagnetic interference, high precision, small size, the potential for remote operation. These advantages are important for applications in areas like biomedical measurement and environmental protection [1,2]. Recently many ways to implement RI sensing is appeared, for example using a SMS fiber based refractometer [2], tapered graded-index polymer optical fibers [3], a Fabry-Perot interferometer [4], a multi-D-shaped optical fiber [5], and holey fiber tapers with resonance transmission [6]

A single mode-gap-multimode-single mode (SGMS) fiber structure is a combination of two different types of optical fiber, where a short length of multimode fiber (MMF) and very short gap are sandwiched between input and output single mode fibers (SMFs) as shown in Fig. (1). The light injected into the input SMF pass throught the gap toward the MMF. Then the light excites multiple modes propagating in the MMF. Interference occurs between these modes (multimode interference "MMI") and as a result, the nature of the light reaching the output SMF is dependent on a number of physical parameters, such as refractive index of gap, refractive index of core, core diameter and the length of the MMF section. This dependence gives SGMS fiber structures great potential for use as sensors, such as refractive index measuring sensor [7,8].

Multimode interference (MMI) in multimode waveguides has interesting self-imaging properties, which have extensively investigated and utilized in many integrated optical devices. Self-imaging can defined as a property of multimode waveguides by which an input field profile is reproduced due to constructive interference to form single or multiple images of the single mode input field at periodic intervals along the propagation direction of the guide. In SGMS fibers structure, the MMI in the multimode section leads to the formation of a self-image of the single mode fiber excitation onto the output single mode fiber core [9].

This paper presents a novel type of optical fiber sensor for measuring refractive index based on an SGMS fiber structure. The simulation of optical field propagation in SGMS fiber structures is obtained by the beam propagation method (BPM). Self-imaging in symmetrically excited multimode optical fibers is simulated to explore the effects of change refractive index in gap on SGMS fiber device characteristics. The SGMS fiber structure is optimized to provide high precision optical fiber sensor for measuring refractive index of fluids.

2. Modeling of Light Propagation in SGMS Structure

The proposed optical fiber sensor consists of SMF, short gap, MMF and SMF. The laser light injected through input SMF then it passes through the gap into MMF fiber. The MMI effect takes place

when light is coupled into the SMF and excites all the modes supported by the MMF. Single images of the SMF input signal will appear along the MMF at periodical intervals along its axis, due to the interference between the modes as they propagate along the MMF [4, 5]

With certain length of MMF, the coupling loss of the SGMS fiber structure depends strongly on the refractive index of gap material but it is also wavelength sensitive. The structure of the proposed optical fiber sensor is shown schematically in Fig. (2). It can note that the gap between the input SMF and MMF and the gap is supposed to be filled by the medium whose RI is to be measured.

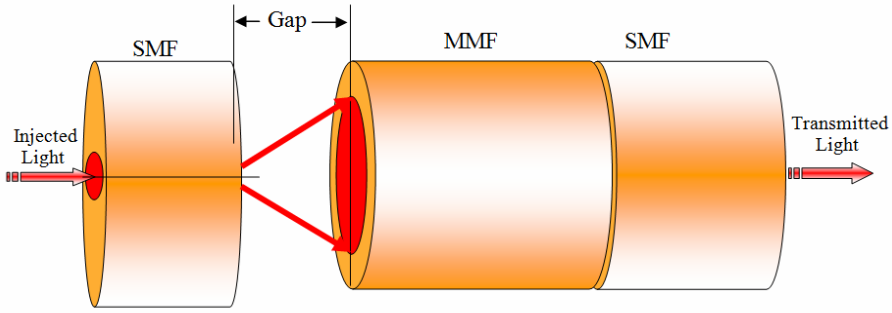

Fig. (1) Single mode-gap-multimode-single mode (SGMS) fiber structure

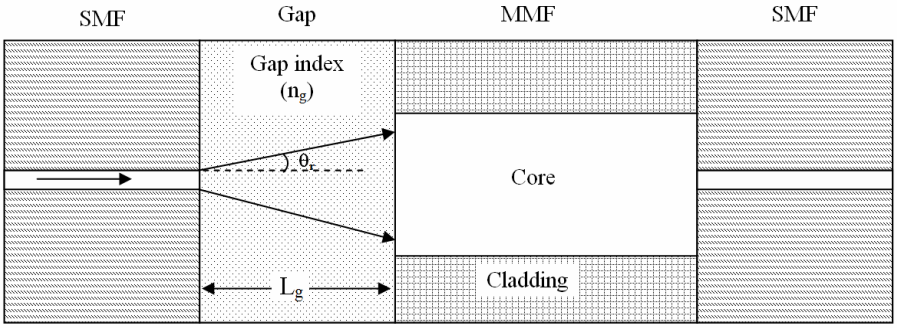

Fig. (2) The structure of the proposed optical fiber sensor

To study the light propagation in SGMS structure, it can assume that the SGMS consist of two sections. First section formed from single mode fiber and gap. Second section formed from whole multi mode fiber and output single mode fiber. In first section, the light pass through the SMF is emitted into the gap according to geometry of optical fiber.

Now consider the geometry of Fig. (2), where a refraction at the fiber–gap interface is occurs, the ray bends faraway from the normal on fiber axis. The angle θ_r of the refracted ray is given by [10]:

$$n_g \cdot \sin\theta_r = \sqrt{n_{SMF}^2 - n_{CLS}^2} \quad (1)$$

and;

$$\theta_r = \sin^{-1}\left(\frac{\sqrt{n_{SMF}^2 - n_{CLS}^2}}{n_g}\right) \quad (2)$$

where n_{SMF} and n_{MMF} are the core refractive index of both SMF and MMF respectively.

It can be calculate the field at end of gap (incident field on the multimode fiber) depends on the input field, the surface areas of the fiber aperture and transmitted beam at end of gap. Therefore, it can express as in the following equation.

$$E_g = E_i \frac{S_f}{S_g} \quad (3)$$

and;

$$S_g = \pi \cdot \left(L_g \cdot \tan(\theta_r)\right)^2 \quad (4)$$

$$S_f = \pi \cdot r_{SMF}{}^2 \quad (5)$$

where E_i is the input field, E_g is the field at end of gap, S_f is Surface area of fiber aperture, S_g is Spot surface at end of gap, r_{SMF} is the radius of the single mode fiber core and L_g is the length of gap

The second section formed the multimode interference. Multimode interference (MMI) in multimode waveguides has interesting self-imaging properties. Therefore, the transmission of multimode–single mode fibers structure can be calculated by [7,9]:

$$L_S(z) = 10\log_{10}\left\{\left|\sum_{m=1}^{M} c_m^2 \exp\left[-i\left(\frac{(2m+1)(2m-1)\pi}{\overline{L_z}}\right)z\right]\right|^2\right\} \quad (6)$$

where c_m is the excitation coefficient of each mode and M is excited mode number of the multimode fiber. It can calculate by:

$m=V/\pi$ (7)

and,

$$V = \frac{2\pi \cdot a\sqrt{n_{MMF}^2 - n_{cl}^2}}{\lambda} \quad (8)$$

where V is the normalized frequency, a is the radius of the multimode fiber core and n_{cl} is refractive index of multimode fiber cladding, and λ is the wavelength of light in the free-space

By substituting in the approximation (6), then it can be rewritten as below:

$$L_s(z) = 10\log_{10}\left(\left|\sum_{m=1}^{M} c_m^2 \exp(-i(2m+1)(2m-1)\pi) g(\lambda, z)\right|^2\right) \quad (9)$$

$$\overline{L_z} = \frac{16\, n_{MMF}\, a^2}{\lambda}$$

where $g(\lambda,z)= \lambda z /16\, n_{co}\, a^2$, and;

$$c_m = \frac{\int_0^{\infty} E_g(r,0) F_m(r) r dr}{\int_0^{\infty} F_m(r) F_m(r) r dr} \quad (10)$$

where $E_g(r,0)$ is the input light to the multimode fiber and F_m is the field profile of LP_{0m} [9]

According to MMI theory, the peak wavelength of a MMI device is given by [8]:

$$\lambda_o = 4p\frac{n_{MMF} \cdot a^2}{L} \quad \text{with p=1, 2, 3} \quad (11)$$

where, L is the length of the MMF and p is the self-image number

As shown in Eq. (11), the peak wavelength response of the MMI section can be selected by simply changing the length of the MMF. An additional advantage when changing the length of the MMF for optimizes the optical response of refractive index sensor where a linear sensing response of the MMI device is obtained.

3. Simulation Results

The proposed SGMS structure formed from standard silica optical fibers. The standard single mode fiber (SMF-28) is chosen as the single-mode fibers, of which the parameters are: the refractive index for the core and cladding is 1.4504 and 1.4447, respectively, at wavelength 1550 nm and 8.3/125 μm core/cladding diameters [9]. The standard multimode fiber has a 62.5μm core/cladding diameters with group index of refraction of 1.491 at 1310 nm [11].

The simulation is done by using BMP software to numerically simulate optical field propagation in different gap length of SGMS fiber structures. According to the simulation results, the MMF length is further optimized to L = 11 mm in order to achieve the best linear characteristics and wider refractive index range at wavelength of 1550 nm.

Figure (3) shows three curves represent the relationship between the power transmission and refractive index with three gap lengths. It can note that, the curve with gap length of L_g=1.5 mm is best linearity over refractive index range of 1.1-1.43. While the curve with gap length of L_g=1 mm has less linearity over refractive index range of 1.26-1.43. Also curve with gap length of L_g=0.75 mm has less linearity over refractive index range of 1.1-1.26. A linear regression method employed to analyze the relationship between sensor response and refractive index changes. This method calculated the best-fitting linear equation (straight line) for the observed data using the least squares approach. Figure(3) shows a linear fit with correlation coefficient R=0.9991 to the plot of sensor response as a function of the refractive index for a sensing fiber with gap length of 1.5 mm. Others curves has correlation coefficients of R=0.9976 and R=0.9991 for gap lengths 1 mm and 0.75 mm, respectively.

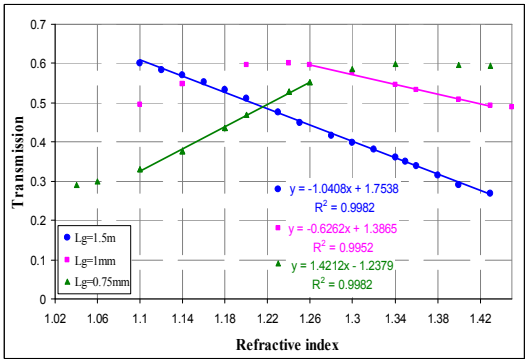

Fig. (3) The relationship between the ratio of power transmission and refractive index with three gap lengths

Figure (4) shows the spectra response of optical sensor with gap length of 1.5 mm as a function of wavelength from 1500 nm to 1600 nm for four refractive indices. It can see that all peaks shift to longer wavelengths as the refractive index of gap is decreased. The shift of the peaks is more remarkable for lower indices. In that range of indices, the intensity of the peaks changes with the refractive index, but their shape approximately remains constant.

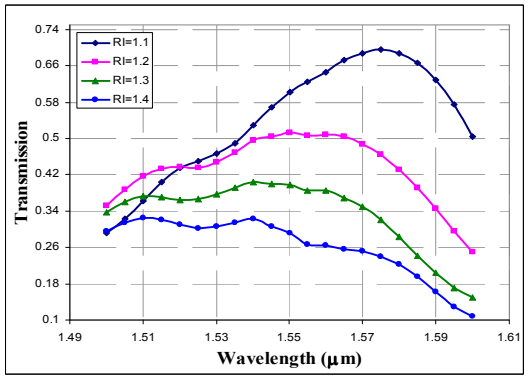

Fig. (4) Power transmission versus the wavelength with various refractive indices for gap length of 1.5mm

The relationship between the power transmitted over the SGMS structure and the refractive index of gap with different wavelength for gap length of 1.5mm is shown in Fig. (5). It can note that the response of optical sensor depends on the wavelength due to the MMI effect. By using a linear regression method to analyze the relationship between sensor response and refractive index changes, it can note that, the sensor response curve with wavelength of 1550 nm is best linearity over refractive index range of 1.1-1.43 with correlation coefficient R=0.9991. While the sensor response curve with wavelength of 1540 nm has less linearity with correlation coefficient R=0.99237. In addition, the sensor response curve with wavelength of 1560nm has less linearity with correlation coefficient R=0.99594. Therefore it can conclude that the proposed optical sensor is operate better at wavelength of 1550 nm with wide range (1.1 -1.43) and best linearity.

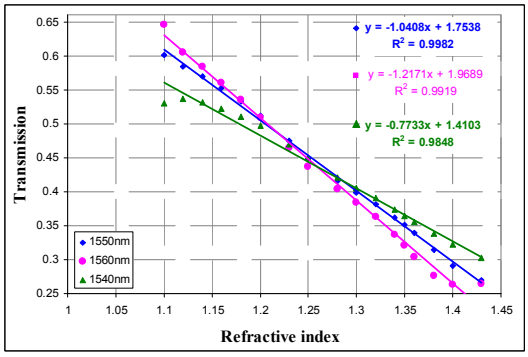

Fig. (5) Power transmission versus the refractive index with different wavelength for gap length of 1.5 mm

Figure (6) represent the field propagation through the SGMS structure for proposed optical sensor (length of MMF is L=11 mm and length of gap is) at wavelengths of 1550 nm with different refractive index of gap. It is clear that (in MMF section) self-imaging of the input field takes place so that at periodic intervals, a single image of the input field is reproduced. This occurs at distances of 3250µm, and 7150 µm measured from input end of MMF fiber at wavelength of 1550 nm. Multi-fold images of the input field can also be found at 1300 µm, 5000 µm, and 8900 µm. Therefore, It can be conclude that, the self-imaging occur at specific lengths only for certain wavelengths.

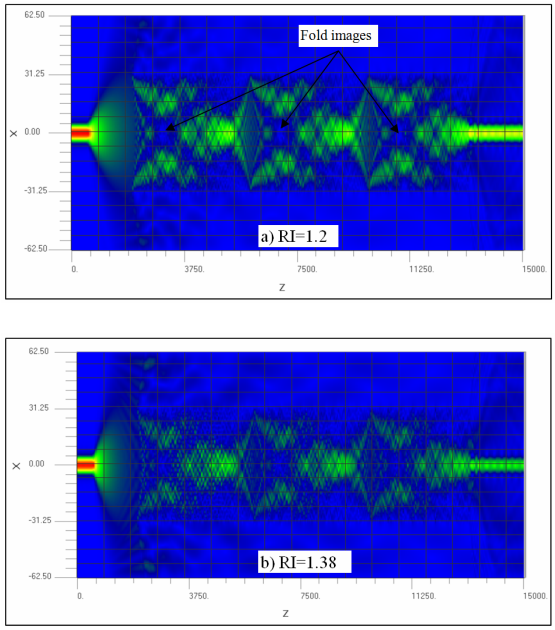

Fig. (6) Propagating fields through proposed optical sensor (a) Propagating fields at 1550 nm with gap refractive index of 1.2 (b) Propagating fields at 1550 nm with gap refractive index of 1.38

Figure (7) shows three curves represent the relationship between the power transmission and refractive index with three multimode fiber lengths at gap length of 1.5 mm over refractive index of 1.1-1.43. It can note that, the curve with MMF length of L=11 mm has best linearity, while the curve with MMF length of L=10.9 mm has less linearity. Also curve with MMF length of L=11.1 mm has less linearity.

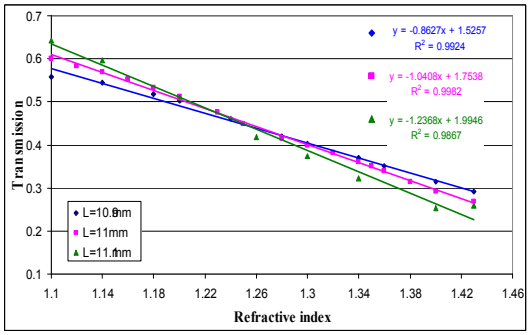

Fig. (7) Represent the relationship between the power transmission and refractive index with various multimode fiber length

By applying a linear regression method to obtain the best-fitting linear equation for the simulated data using the least squares approach. Figure (7) shows a linear fit with correlation coefficient R=0.9991 to the plot of sensor response as a function of the refractive index for a sensing fiber with MMF length of 11 mm. Others curves has correlation coefficients of R=0.9962 and R=0.9933 for MMF lengths 10.9mm and 11.1mm respectively. That is the reason why the length of the multimode fiber is chosen equal to 11 mm rather than 10.9 mm or 11.1 mm for proposed optical filter.

4. Conclusion

In conclusion, a simple optical fiber sensor for refractive index measurements based on the MMI phenomenon of self-imaging was demonstrated. The optical sensor was utilized compose of single mode-gap-multimode-single mode fiber structure. The power transmission of optical fiber sensor was plotted, from which the device was found to be suitable for refractive index sensor.

The proposed refractive index sensor is utilized standard optical fibers; therefore, the light source and the fiber used in sensor are compatible with the low-cost 1550nm optical communication technology. Additionally, the device is quite simple and relatively inexpensive when compared with other optical sensor techniques. The results reported here demonstrate that the SGMS fiber sensor is attractive for chemical, biological, and biochemical sensing with aqueous solutions further than it may used in gas refractive index sensing.

References

[1] Z.L. Ran et al., "Laser-micromachined Fabry-Perot optical fiber tip sensor for high-resolution temperature independent measurement of refractive index", *Optics Express*, 16(3) (2008) 2252-2263.

[2] Q. Wu et al., "High sensitivity SMS fiber structure based refractometer – analysis and experiment", *Optics Express*, 19(9) (2011) 7937-7944.

[3] J. Arrue et al., "Analysis of the use of tapered graded-index polymer optical fibers for refractive index sensors", *Optics Express*, 16(21) (2008) 16616-16631.

[4] Y. Tian et al., "A Miniature Fiber Optic Refractive Index Sensor Built in a MEMS-Based Microchannel ", *J. Sensors,* 11(1) (2011) 1078-1087.

[5] C.-H. Chen et al., "A Multi-D-Shaped Optical Fiber for Refractive Index Sensing", *J. Sensors*, 10(5), (2010) 4794-4804.

[6] V.P. Minkovich et al., "Holey fiber tapers with resonance transmission for high-resolution refractive index sensing", *Optics Express*, 13(19) (2005) 7609-7614.

[7] L.B. Soldano and E.C.M. Penning, "Optical Multimode Interference Devices Based on Self-Imaging: Principles and Applications", *J. Lightwave Technol.*, 13(4), (1995) 615-627.

[8] A. Castillo-Guzman et al., "Widely Tunable Erbium-Doped Fiber Laser Based on Multimode Interference Effect", *Optics Express*, 18(2) (2010) 591-597.

[9] Q. Wang et al., "Investigation on single mode-multimode-single mode fiber structure", *IEEE J. Lightwave Technol.*, 26(5) (2008) 512-519.

[10] G.P. Agrawal, **"Fiber-Optic Communication Systems"**, John-Wiley & Sons Inc., (2002), Ch. 2, p. 25.

[11] Draka.com, "C02: General purpose multimode 62.5µm fiber", www.draka.com/communications, C02_e, 2010, version 10.

This article was reviewed at School of Electronic Engineering and Computer Science, Peking University, CHINA and School of Applied Sciences, University of Technology, Baghdad, IRAQ

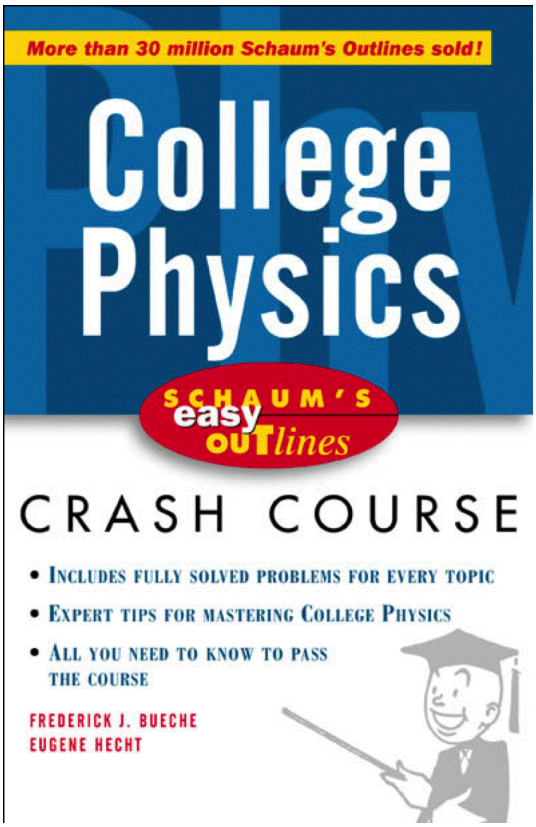

SCHAUM'S *Easy* OUTLINES

COLLEGE PHYSICS

BASED ON SCHAUM'S *Outline of College Physics*
BY FREDRICK J. BUECHE AND EUGENE HECHT

ABRIDGEMENT EDITOR:
GEORGE J. HADEMENOS

SCHAUM'S OUTLINE SERIES
McGRAW-HILL

New York San Francisco Washington, D. C. Auckland Bogotá Caracas Lisbon London Madrid Mexico City Milan Montreal New Delhi San Juan Singapore Sydney Tokyo Toronto

Contents

Design and Simulation of Q-Switching and Mode-Locking Nonlinear Mirror for Frequency-Doubled DPSS Nd:YAG Laser Output

Aseel A. Al-Sharify

Department of Laser and Optoelectronics Engineering, University of Technology, Baghdad, IRAQ

In this work, multilayer reflection coating analysis has been employed for designing and simulating nonlinear mirror to be used for Q-switching and mode-locking of frequency-doubled DPSS Nd:YAG laser using composite crystal (DPM010X). It was found that the optical reflection greatly depends on the type of the nonlinear crystal and dichroic material used, the type of the refractive index (ordinary or extra-ordinary), direction of propagation inside the nonlinear material, optical thickness and the number of anti-reflection coating layer used. The calculated refracted index was found to be 2.232 for the 1064nm wavelength for $LINBO_3$ crystal and 1.655 for 1064nm for the BBO crystal. The results show that the reflectivity reaches the best value when the refractive index difference between the anti-reflection coating layers is small, and increasing the number of such layer. The calculated phase-match angle is equal to 13.75177°.

Keywords Nd:YAG Laser, Second Harmonic Generation, Nonlinear Mirror, Mode Locking
Received: 19 July 2011, **Revised**: 15 October 2011, **Accepted**: 22 October 2011

1. Introduction:

Diode-Pumped Solid State (DPSS) lasers are the ideal laser tools of machining, material processing, spectroscopy, wafer inspection, light show, medical diagnostics and other applications. The DMP110X composite crystals which combine the vanadate (Neodimium Doped Yttrium Aluminum Garnet) Nd:YAG and non-linear crystals. The DPM crystals are mainly used for low power applications, for example, the Green Laser Pointers. Here are some systems that will get you some green light without either expensive crystals or the need for complex mounting and infinite alignment fiddling, as shown in Fig. (1). I am, of course, talking about the use of a hybrid (also called composite) vanadate-non-linear crystal. A non-linear mirror consisting of a non-linear crystal and a dichroic output coupler are used to mode-lock (passively) an Nd:YAG laser, pumped by a diode laser.

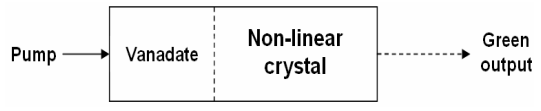

Fig. (1) Schematic diagram of the (DPM) composite crystal [1]

2. Theory

The Solid State (SS) Laser uses a solid crystalline material as the lasing medium and is usually optically pumped. Nd:YAG is one of the most efficient laser crystal for diode laser-pumped solid-state lasers especially used in end-pumping configurations. This laser crystal is finding much use in frequency doubled green laser pointers and other small diode laser modules.

Second Harmonic Generation (SHG) occurs an intense light beam of angular frequency ω passing through an appropriate crystal (e.g. KTP) generates a light beam of double the frequency, ω_2 If E is the electric field in the light wave, then the induced polarization P becomes a function of E and can be written as

$$P = \varepsilon_\circ \chi_1 E_\circ \sin(\omega t) - \tfrac{1}{2}\varepsilon_\circ \chi_2 E_\circ \cos(2\omega t) + \tfrac{1}{2}\varepsilon_\circ \chi_2 E_\circ$$

where χ_1, χ_2 and χ_3 and are the linear, second-order and third-order susceptibilities

SHG is based on a finite χ_2 coefficient in which the effect of χ_3 is negligible. The first term is the fundamental, second is the second harmonic and third is the dc term. The second harmonic (2ω oscillation of local dipole moments generates secondary second harmonic (2ω) waves in the crystal as shown in Fig. (2). However, the crystal will normally possess different refractive indices n(ω) and n(2ω) for frequencies ω and 2ω. The condition that the second harmonic waves must travel with the same phase velocity as the fundamental wave to constitute a second harmonic beam is called phase matching and requires $n(\omega)=n(2\omega)$. One method is to use a birefringent crystal as these have two refractive indices: ordinary index no and extraordinary index n_e. Suppose that

along a certain crystal direction at an angle θ to the optic axis, $n_e(2\omega)$ at the second harmonic is the same as $n_o(\omega)$ at the fundamental frequency: $n_e(2\omega)=n_o(\omega)$. This is called index matching and the angle θ is the phase matching angle. To separate the second harmonic beam from the fundamental beam, something like a diffraction grating, a prism or an optical filter (such as anti reflection coating) will have to be used at the output as. The optical matrix approach was employed for N-layer design of antireflection coating the main idea of this method is matching the E and H fields of the incident light on the interfaces of the multilayer optical coatings .the matrix relation defining the N-layer antireflection problem is given by [1]

$$\begin{bmatrix} B \\ C \end{bmatrix} = \prod_{qi=1}^{m} \begin{bmatrix} \cos\delta_q & i\sin\dfrac{\delta_q}{n_q} \\ in_q \sin\delta_q & \cos\delta_q \end{bmatrix} \begin{bmatrix} 1 \\ n_s \end{bmatrix} \quad (1)$$

where B and C are total electric and magnetic field amplitudes of light propagation in the medium .thus optical admittance is given by the ratio

$$Y = \frac{C}{B} \quad (2)$$

where n is the refractive index of the layer and δ is the phase thickness given by

$$\delta = \frac{2\pi n d_q}{\lambda} \quad (3)$$

with the physical thickness of the layer being d_q, then the reflection coefficient r and the reflectivity R are , respectively , given by [1]

$$R = r x r^* \quad (4)$$

where r is the reflectance

$$r = \frac{n_0 - Y}{n_0 + Y} \quad (5)$$

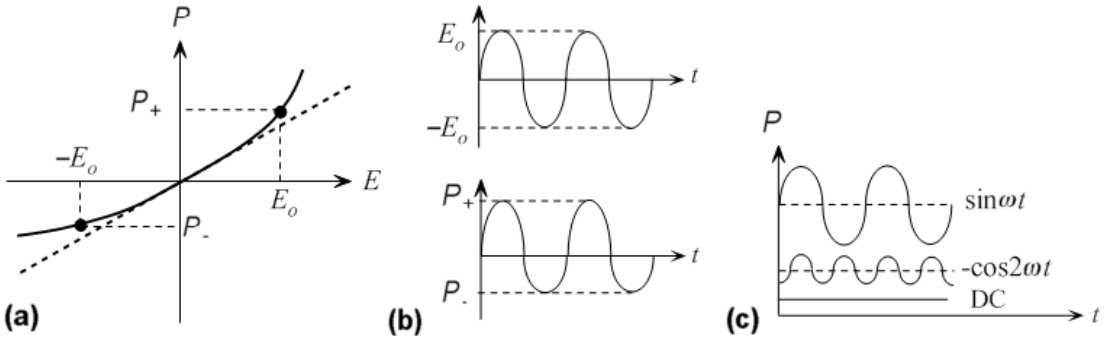

Fig. (2) (a) Induced polarization vs. optical field for a nonlinear medium. (b) Sinusoidal optical field oscillation between E_o result in polarization oscillation between P_+ and P_-. (c) The polarization oscillation can be represented by sinusoidal oscillations at angular

The laser is operated in actively Q-switched mode to obtain nanosecond pulse by inserting an acousto-optic Q-switch in the laser cavity [2]. Whereas, nonlinear mirror (NLM) technique is used to realize passive mode-locking for the generation of picosecond pulses. In NLM systems, a frequency doubling nonlinear crystal (NLC) is incorporated in the laser cavity and placed near a dichroic mirror used in place of the usual output coupler. The dichroic mirror partially reflects the fundamental wave (FW) but totally reflects the second harmonic (SH) beams. The FW generates SH in its first pass and if the SH beam experiences a proper phase shift with respect to the FW beam, the SH power is almost totally reconverted into FW during the second pass through the NLC. As the second harmonic generation (SHG) is a second order nonlinear optical process, the NLC along with the dichroic mirror behaves as a NLM having an intensity dependent reflection coefficient. Under this condition the laser losses decrease with an increase in the peak power of the FW beam and so the behavior is the one of a fast saturable absorber. The nonlinear mirror initiates the generation of ultrashort pulse. The advantage of this mode-locking over semiconductor saturable absorber is its simplicity in design and can be operated in wide spectral range [3].

3. Experiment

(DPM1101) composite crystal in Diode-Pumped Solid State (DPSS) lasers system has been chose for designing the required model .The use of hybrid or composite crystals represents by far the easiest way to construct a low power green DPSS laser. They virtually eliminate fiddling as a pastime since the HR, Nd:YAG (vanadate), non-linear crystal , and OC mirrors are all permanently aligned. For many applications, no additional optics is required. Such systems are used mainly for SHG, which involve two fundamental mode photons[4].

The specifications of the DPM crystal 1101 are summarized by:

- **Size and finish:** The DPM0101 is approximately 1x1x2.5 mm (WxHxL).
- **Vanadate doping and thickness:** The doping is probably 3 percent and the thickness is 0.5 mm.
- **Vanadate features and optical properties :** The main feature of the vanadate is :
  1- Low lasing threshold and high slope efficiency.
  2- Large stimulated emission cross-section at lasing wavelength.
  3- High absorption over a wide pumping wavelength bandwidth.
  4- Optically uniaxial and large birefringence emits polarized laser. Its Fluorescence Spectra Curve are shown below in Fig. (3) [5].

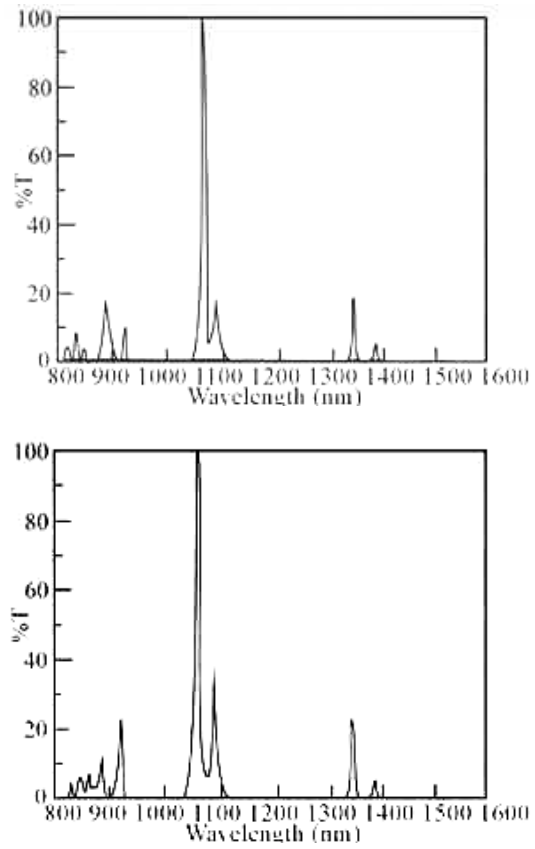

Fig. (3) Fluorescence Spectra Curve of the vanadate

Because of its large stimulated emission cross section at 1.34 mm, Nd:YAG is also an efficient laser crystal for diode laser-pumped 1.3 mm laser [5]. By using the compact design of Nd:YAG non linear crystal crystals, high power green or red light output can be generated in a diode laser pumped Nd:YAG laser. The optical properties of the Vanadate are shown in table (1) [6].

4. Simulation in MATLAB:

The simulation of the reflection in MATLAB have been the main assignment of this work, the reflectivity of non linear mirror have been simulated with multilayer antireflection coating after chose the proper type of material for both high and low index of reflection which must has suitable absorption, good adhesion, low stress, hardness and low cost and easy preparation. The program optimize at λ_0=532 nm central wave length for visible and near infrared spectral region (300-1100) nm. The parameters of antireflection are:

1- Optical thickness for each layer
2- Refractive index for each layer coating and substrate

The material must be select that low wave absorption, homogeneity, high packing density, good adhesion, low stress, hardness, and ability survive in deferent environmental, low cost and easy preparation [7-8].

5. Results and Discussion

Reflection was taken as function of the wave length for different type of coated material for non linear mirror as shown below. non linear crystal was taken as substrate material with refractive index of (2.2082) for the ($KNbO_3$) and (1.6551) for the (BBO) crystal, reflection has been simulated with central wavelength (532nm) which is the second harmonic one , in the range begun from visible up to near IR range in multilayer anti-reflection technique, as shown in the following simulated figures. The thickness of the layer was taken equal to 0.25 of wavelength because it's the perfect one .Different type of dichroic material were taken in the simulation in order to reach to the perfect one .

In all simulated figures below, N values strongly affected on the reflectivity .increasing N increased proper choice to reach to the required situation for example in our design for the non linear mirror HR was needed for the 532nm and HT for the 1064nm [7] this can be take with N=12 in all curve, we notes also that there are much difference in the reflectivity behavior seen resulting from changing optical thickness of the anti-reflected coating that's affected on the design requirement which is one of the most important factor that's limit our design and make as carefully choosing its value this not only note but its really bright point leading us to choose the good design parameter if we compares between all figures with Fig. (10) by which we can believe that 0.25 optical thickness value is the more suitable one for this work. finally the proper choice for the antireflection layer material is critical point not only because its refractive index which effect on reflectivity value but its limit the life time of our design because the other property of it, such as stress, hardness and ability to survive in different environmental, cost and preparation ability.

Table [1] optical properties of the Vanadate [6]

Lasing Wavelengths	914nm, 1064 nm, 1342 nm
Crystal class	positive uniaxial, $n_o=n_a=n_b$, $n_e=n_c$
Sellmeier Equation (for pure YAG crystals): $n_o^2=3.77834+0.069736/(\lambda^2 - 0.04724) - 0.0108133.\lambda^2$ $n_e^2=4.59905+0.110534/(\lambda^2 - 0.04813) - 0.0122676.\lambda^2$	
Thermal Optical Coefficient:	$dn_a/dT=8.5x10^{-6}/K$, $dn_c/dT=3.0x10^{-6}/K$
Stimulated Emission Cross-Section	$25.0x10^{-19}$ cm^2 , @1064 nm
Fluorescent Lifetime	90 µs (about 50 µs for 2 atm% Nd doped) @ 808 nm
Absorption Coefficient	31.4 cm^{-1} @ 808 nm
Absorption Length	0.32 mm @ 808 nm
Diode Pumped Optical to Optical Efficiency	> 60%

Optical Properties

Transparency Range:	400 - 4500 nm			
Absorption loss:	<=1%/cm at 1064nm			
Damage threshold:	<=4J/cm^2 at 527nm (500ps, single pulse)			
	<=6J/cm^2 at 1054nm (700ps, single pulse)			
Principal Axes Û Crystallographic Axes:	x Û c; y Û a; z Û b (ie. $n_b>n_a>n_c$)			
Typical Refractive Indices:	¡¡	n_a (n_y)	n_b (n_z)	n_c (n_x)
¡¡	430nm	2.4145	2.4974	2.2771
¡¡	532nm	2.3223	2.3813	2.2022
¡¡	860nm	2.2372	2.2784	2.1338
¡¡	1064nm	2.2195	2.2576	2.1194
Sellmeier Equations: (l in mm)				
$n = 4.4208 + 0.10044/(l^2 - 0.054084) - 0.019592l^2$ $n = 4.8355 + 0.12839/(l^2 - 0.056342) - 0.025379l^2$ $n = 4.9873 + 0.15149/(l^2 - 0.064143) - 0.028775l^2$				

Nonlinear Optical Properties

Nonlinear Optical Coefficients:	d_{31}=-15.8pm/V, d_{32}=-18.3pm/V at 1064 nm
The Shortest SHG Wavelength:	425 nm (type I NCPM, y-cut or a-cut)
Acceptance Angle for Type I SHG of 1064 nm:	Dq = 0.24 mrad-cm (internal)

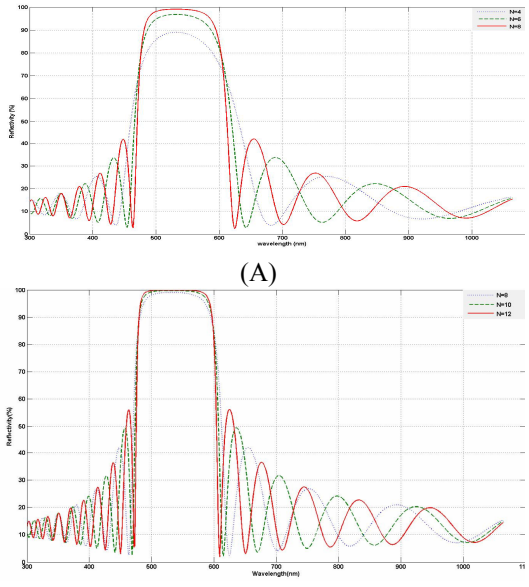

(A)

(B)

Fig. (4) Reflection as function of wavelength for (Tio_2 as high index) and (MgO as low index) coated material and (KNbO 3)as non linear crystal. (A) simulated figure with optical thickness (N=4,6,8) for both high and low coated layer. (B) simulated figure with optical thickness (N=8,10,12) for both high and low coated layer.

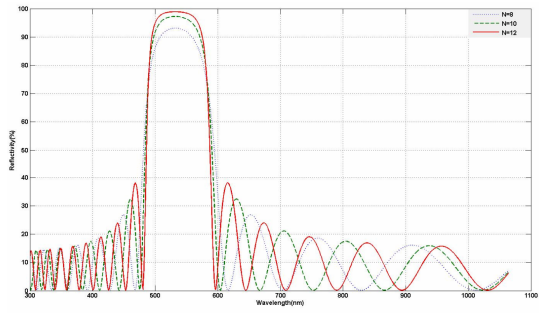

Fig. (5) Reflection as function of wavelength for (MgO as high index) and (MgF_2 as low index) coated material and(KNbO 3)as non linear crystal

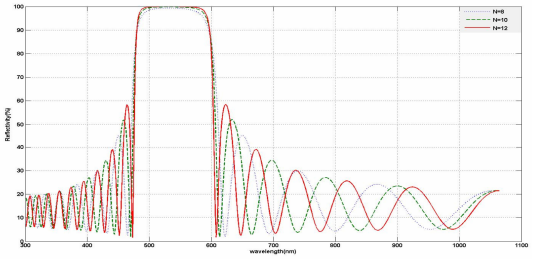

Fig. (6) Reflection as function of wavelength for (TiO_2 as high index) and (MgO as low index) coated material and(BBO)as non linear crystal

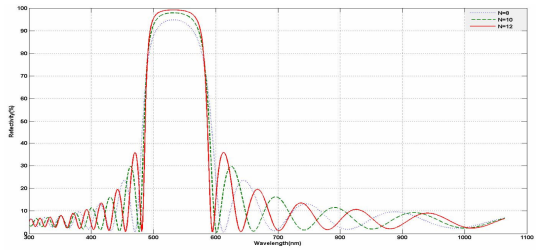

Fig. (7) Reflection as function of wavelength for (MgO as high index) and (MgF_2 as low index) coated material and(BBO)as non linear crystal

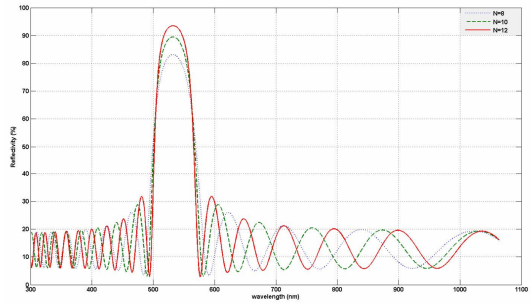

Fig. (8) Reflection as function of wavelength for (ZrS as high index) and (SiO as low index) coated material and(BBO)as non linear crystal

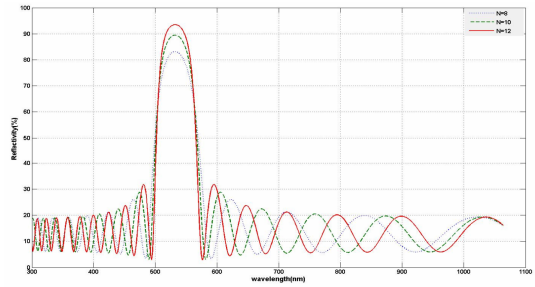

Fig. (9) Reflection as function of wavelength for (ZrO_2 as high index) and (HfO_2as low index) coated material and(BBO)as non linear crystal

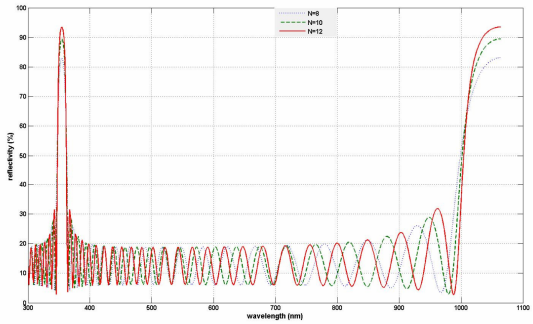

Fig. (10) Reflection as function of wavelength for (ZrO_2 as high index) and (HfO_2as low index) coated material and(BBO)as non linear crystal with half wavelength thickness

6. Conclusion:

We can say that the best choice for the N is 12 with 0.25 optical layer thickness by which the design reaches the optimum requirement and the material used as a layer in Fig. (9) is the best because it makes design approaches the required as the reflectivity for the 532nm is 93% and for the 1064nm is 18% and the band of tuned wave length is very small. All thesemake this design parameter is nearly the perfect.

References

[1] Macleod, H.A., **"Thin–Film Optical Filters"**, 2nd ed., 2001, Bristol Co., Ltd. (UK).

[2] P.K. Datta et al., *Optics Express*, 12, 4041 (2004).

[3] T.R. Schibli et al., *Appl. Phys. B*, 70, 41 (2002).

[4] M. Lipinski et al., *Materials Science –Poland*, 24(4) (2006) 13-22.

[5] M.M. Fejer et al., *IEEE J. Quantum Electron.*, QE-28, 2631–2654 (1992).

[6] R. Dabu, C. Fenic and A. Stratan, *Optica Applicata*, XXVI(3), 171–183, (1996).

[7] H.E. Selhofer and R. Linsbod, *Appl. Opt.*, 41 (2002) 756.

[8] J.M. Bennett, et al., *Appl. Opt.*, 28 (1989) 3303.

This article was reviewed at Department of Physics, Faculty of Science, Tsinghua University, CHINAand Department of Physics, College of Education, The Iraqi University, Baghdad, IRAQ

Engineering Materials 1

An Introduction to their Properties and Applications
Second Edition

by
Michael F. Ashby
David R. H. Jones

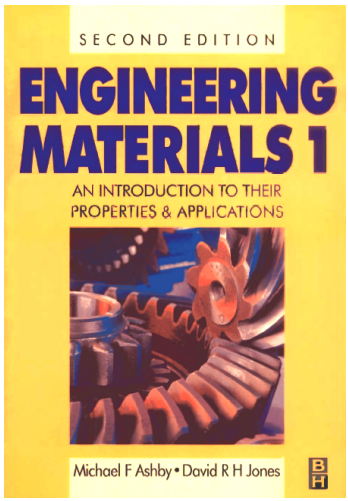

To the student

Innovation in engineering often means the clever use of a new material - new to a particular application, but not necessarily (although sometimes) new in the sense of 'recently developed'. Plastic paper clips and ceramic turbine-blades both represent attempts to do better with polymers and ceramics what had previously been done well with metals. And engineering disasters are frequently caused by the misuse of materials. When the plastic tea-spoon buckles as you stir your tea, and when a fleet of aircraft is grounded because cracks have appeared in the tailplane, it is because the engineer who designed them used the wrong materials or did not understand the properties of those used. So it is vital that the professional engineer should know how to select materials which best fit the demands of the design - economic and aesthetic demands, as well as demands of strength and durability. The designer must understand the properties of materials, and their limitations.

This book gives a broad introduction to these properties and limitations. It cannot make you a materials expert, but it can teach you how to make a sensible choice of material, how to avoid the mistakes that have led to embarrassment or tragedy in the past, and where to turn for further, more detailed, help. You will notice from the Contents list that the chapters are arranged in *groups,* each group describing a particular class of properties: the elastic modulus; the fracture toughness; resistance to corrosion; and so forth. Each such group of chapters starts by *defining the property,* describing how it is *measured,* and giving a table of *data* that we use to solve problems involving the selection and use of materials. We then move on to the *basic science* that underlies each property, and show how we can use this fundamental knowledge to design materials with better properties. Each group ends with a chapter of *case studies* in which the basic understanding and the data for each property are applied to practical engineering problems involving materials. Each chapter has a list of books for *further reading,* ranked *so* that the more elementary come first.

At the end of the book you will find sets of examples; each example is meant to consolidate or develop a particular point covered in the text. Try to do the examples that derive from a particular chapter whiles this is still fresh in your mind. In this way you will gain confidence that you are on top of the subject. No engineer attempts to learn or remember tables or lists of data for material properties. But you *should* try to remember the broad orders-of-magnitude of these quantities. All grocers know that 'a kg of apples is about 10 apples' - they still weigh them, but their knowledge prevents them making silly mistakes which might cost them money. In the same way, an engineer should know that 'most elastic moduli lie between 1 and lo3G N m-2; and are around 102GNm W2fo r metals' - in any real design you need an accurate value, which you can get from suppliers' specifications; but an order-of-magnitude knowledge prevents you getting the units wrong, or making other silly, and possibly expensive, mistakes. To help you in this, we have added at the end of the book a list of the important definitions and formulae that you should know, or should be able to derive, and a summary of the orders-of-magnitude of materials properties.

To the lecturer

This book is a course in Engineering Materials for engineering students with no previous background in the subject. It is designed to link up with the teaching of Design, Mechanics and Structures, and to meet the needs of engineering students in the 1990s for a first materials course, emphasising applications.

The text is deliberately concise. Each chapter is designed to cover the content of one 50-minute lecture, twenty-seven in all, and allows time for demonstrations and illustrative slides. A list of the slides, and a description of the demonstrations that we have found appropriate to each lecture, are given in Appendix 2. The text contains sets of worked case studies (Chapters 7, 12, 16, 20, 22, 24, 26 and 27) which apply the material of the preceding block of lectures. There are examples for the student at the end of the book; worked solutions are available separately from the publisher.

We have made every effort to keep the mathematical analysis as simple as possible while still retaining the essential physical understanding, and still arriving at results which, although approximate, are useful. But we have avoided mere description: most of the case studies and examples involve analysis, and the use of data, to arrive at numerical solutions to real or postulated problems. This level of analysis, and these data, are of the type that would be used in a preliminary study for the selection of a material or the analysis of a design (or design-failure). It is worth emphasising to students that the next step would be a detailed analysis, using *more* precise *mechanics* (from the texts given as 'further reading') and *data from the supplier* of *the material or from in-house testing.* Materials data are notoriously variable. Approximate tabulations like those given here, though useful, should never be used for final designs.

Gamal A. El-Sayed
Rami M. Basyouni

Department of Physics, College of Science, Almenofiya University, Almenofiya, EGYPT

Light-Beam-Induced-Current Analysis of Thin-Film Polycrystalline Solar Cells

Light-beam-induced-current (LBIC) measurements are providing a direct link between the spatial non-uniformities inherent in thin-film polycrystalline solar cells, such as CdTe and CIGS, and the overall performance of these cells. LBIC is uniquely equipped to produce quantitative maps of local quantum efficiency with relative ease. Spatial resolution of 1 μm at 1-sun intensity, and return to the same area after other measurements, is routinely achieved. A wavelength range of 638nm to 857nm is available with diode lasers. The LBIC measurements demonstrate that several types of effects that alter cell performance can be traced to specific local-area features. Examples of such effects include defects related to edges, grids, or scribes, spatial variations in alloying, and local changes due to high-temperature stress.

***Keywords*:** Thin Films, LBIC Analysis, Polycrystalline Solar Cells, CIGS
Received: 18 March 2011, **Revised:** 25 August 2011, **Accepted:** 2 September 2011

1. Introduction

Since the late 1970's, scanned laser beams have been used to measure photocurrent variations in multicrystalline silicon cells [1-3]. In the 1980's, the two-dimensional laser scanner, which used oscillating mirrors to produce a rastered response map, was developed and used to map defects in thin-film solar cells [4]. Improvements to the two-mirror scanner reduced the laser spot size to 2 μm [5] and introduced modern computer techniques to capture and store the data [6]. The two-mirror scanner, however, is not well suited to quantitative studies of small areas, since it is difficult to align and to maintain a highly focused spot over a significant area.

Instead of moving a laser beam across a solar cell, the cell can also be moved through a fixed the laser beam, either with translation stages [7] or with pieozoelectric rastering [8]. Use of a modern stepper motors makes the translation-stage approach straightforward, and one can reliably position and reposition a specific area within the beam with uncertainty much less than 1 μm. It is highly desirable to be able focus the laser beam near its diffraction limit and to maintain an intensity similar to normal solar intensity. These requirements imply a laser-beam power the order of 1nW, which produces photocurrents the order of 1nA.

2. Light-Beam-Induced-Current System

The Light-Beam-Induced-Current (LBIC) configuration used to measure solar-cell response is shown in Fig. 1 [9-11]. A similar LBIC facility has been reported in Ref. [12]. In Fig. (1), the light source is selected from laser diodes of different wavelengths between 638 and 850 nm. Current to the laser diode is electronically modulated to produce an AC laser beam, and the modulation also provides the reference signal for a lock-in amplifier. Attenuation over a wide dynamic range is set with digital control. The beam is expanded, the s-polarization is selected, and the beam is sampled for both intensity and back-reflection from the cell. Beam steering mirrors allow a parallel beam to impinge on the objective lens (Olympus 1-UB367 SL C Plan Fluoride 40x/0.55 N.A.). This lens is equipped with a correction collar to focus through 0 – 2.5 mm of glass. It has a working distance of 8.8 mm, which allows ample room for contacts.

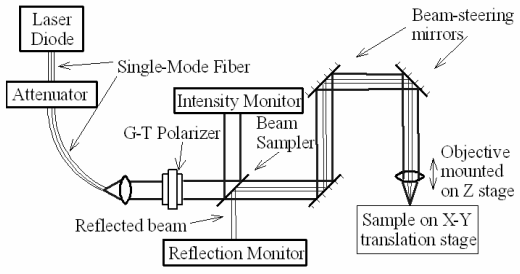

Fig. (1) Schematic of Light-Beam-Induced-Current LBIC apparatus

LBIC measurements using the apparatus shown in Fig. (1) are made by stepping the solar cell under study through the focused beam in a raster pattern. The stepping distance is generally set to half the beam size. Data collection takes approximately 20 min to produce a photocurrent map of 101 by 101 points for a small area, and somewhat longer for larger areas requiring greater travel distances.

3. Data Presentation

Our LBIC data is commonly presented in one of three formats as illustrated in Fig. (2). The top figure shows an intensity projection of a CIGS solar cell with the grid fingers clearly visible. The middle figure for the same cell is the most common format, the local-area quantum-efficiency (QE) map of the area of interest. This format clearly illustrates an isolated feature with low response. The bottom format repeats the same CIGS data in a histogram format, which more clearly emphasizes the spread in QE over the cell.

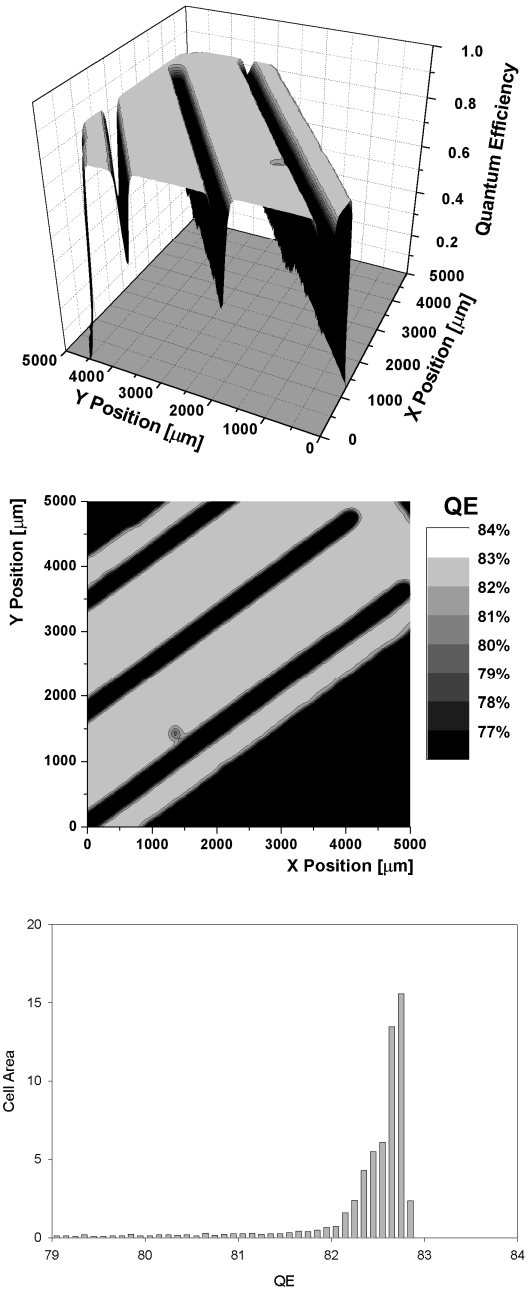

Fig. (2) Three LBIC formats (low resolution)

Three standard resolutions are used, and these are illustrated in Fig. (3) for an NREL-manufactured CIGS cell. Low resolution, shown at the top, has a 5mm field and a 100μm spot. This resolution often covers a significant portion of a typical test cell. The small square in this view is magnified ten times for the middle map at mid resolution (500 by 500μm field and 10μm spot). The area shown in that map's small square in multiplied 10 times more for the 50 by 50 μm field with a 1 μm spot for the high resolution map at the bottom of Fig. (3).

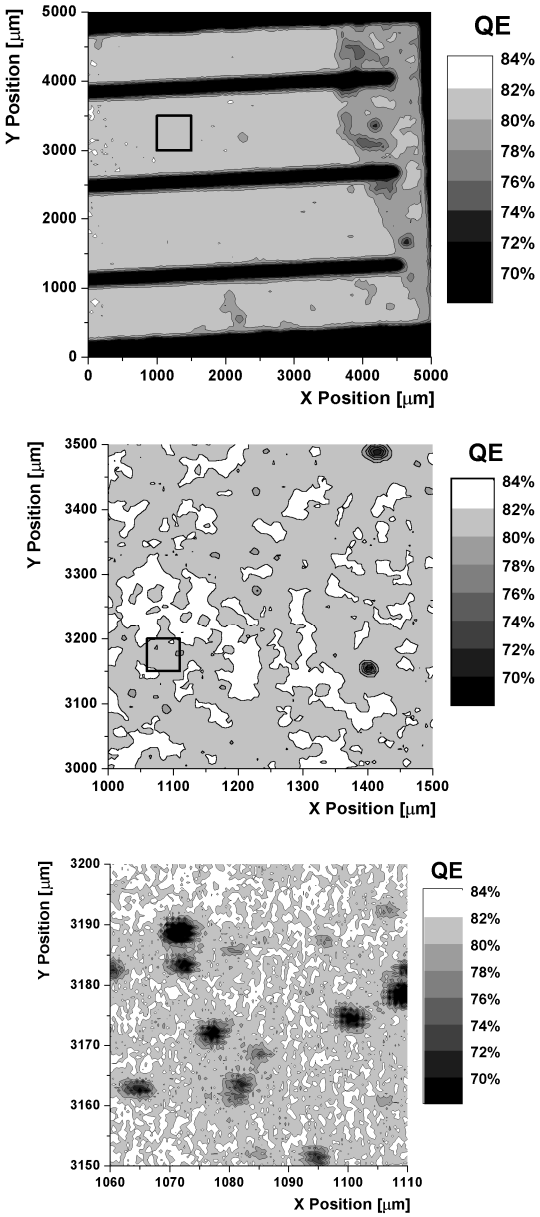

Fig. (3) LBIC with low-, mid-, and high-resolution (100-, 10-, and 1-micron spots)

In each case the beam was attenuated so that intensity at the cell was comparable to one sun. This process makes it straightforward to zoom in on a small area of particular interest and to return to the same area even after the cell has been removed from the apparatus for other measurements. The bottom high-resolution map,

for example, shows several features that are 2-5 microns in dimension that are only marginally seen at lower resolution.

The quantum-efficiency maps shown in Fig. (3) all have a scale to show QE changes of 2%. This scale is varied as needed to match the total variation of interest. For example, 1% gradations were used in the middle section of Fig. (2). In general, the average QE of the LBIC maps agrees quite well with QE measured with a conventional system. All of the data shown in Figs. (2) and (3) were taken at zero bias and a wavelength of 638 nm, which will be taken as standard unless otherwise stated.

The most common LBIC features are local optical blockages that reduce the photocurrent over small, well-defined areas. Their characteristic signature is sharp edge definition, and they can result from inclusions during fabrication. They are most likely what is seen in the middle section of Fig. (2) and the bottom section of Fig. (3). In some cases, there is an accompanying increase in reflection that gives a nearly identical map over the same area. There are two other possibilities, however, which have a similar signature to an optical impediment. One is a local area that does not collect photocarriers efficiently, and the other is a region where adjacent layers have not made good electrical contact. The latter situation often extends over larger regions than the features seen in Figs. (2) and (3).

The second major category of LBIC features is a leakage path, which could be either a filamentary shunt or a weak diode. The latter tends to be very bias dependent. In either case, the actual flaw can be very small, but the photocurrent reduction will spread over a much larger area.

A third category of LBIC features is what we term external. These features can result, for example, from blemishes in a flexible substrate, from the pressure applied by measurement probes, or simply from dust particles on the surface. One consequence of the large number of possibilities for LBIC features is that it is rare to find a cell, even the best space-qualified cell, where the LBIC map is completely uniform.

LBIC measurements are particularly valuable to help explain changes sometimes seen in CdTe solar cells that have been subjected to elevated-temperature stress. The general observation is that when the performance of a cell changes during such stress, the changes are essentially never uniform over the entire cell. The result is an increase in the non-uniformity seen in LBIC measurements. An example is given in Fig. 5, which shows a low-resolution, whole-cell map before any stress, after 8 hours, and after 8 days at a temperature of 100ºC under illumination and short circuit conditions. The average QE decreased by about 2% over 8 days, which is reflected in the current-voltage (J-V) curve, but there were small areas where the reduction was significantly larger.

In many cases, the impact of elevated-temperature stress on both J-V and LBIC data varies significantly with differences in cell fabrication. One example reported earlier [13] was much larger non-uniformities generated in CdTe cells made with insufficient copper in the back contact. Another example, illustrated in histogram format in Fig. (4), contrasts two CdTe cells that differed in another aspect of fabrication. Both cells had very uniform QE initially. After exposure to 30 days of elevated-temperature stress, the cell in the top panel with standard back-contact processing showed only a modest decrease in average QE and uniformity. However, the cell depicted in the bottom QE histogram, which was made with part of the contact procedure omitted, showed much larger reductions in both the magnitude and uniformity of its QE.

4. Wavelength and Bias Variations

The ability to vary the wavelength used for LBIC measurements is particularly valuable if wavelength can be scanned through the absorber band gap. One of our laser diodes was chosen so that its wavelength could be varied from 830 to 860 nm, which spans the CdTe band gap, by varying its temperature. An earlier report [10] showed that this technique could be used with high-resolution LBIC to observe the band-gap variations due to spatial variations in CdTe/CdS mixing.

Variations of LBIC maps as a function of cell bias has also proven useful. In this case, improvements in the detection electronics were required to adequately separate the ac LBIC signal from the dark dc response of the cell. With care, LBIC data can now be taken at bias up to the cell's open-circuit voltage.

An example of LBIC bias dependence is shown in Fig. (5). The top figure shows the J-V curve from two CIGS cells made with different concentrations of gallium. The cell with the better-behaved J-V curve had a uniform LBIC response at all biases. The magnitude of the LBIC signal, however, did decrease when the J-V curve turned up following the expected behavior of the apparent quantum efficiency [14]. The mid-resolution LBIC response from the "distorted" J-V curve (Fig. 5), however, showed a decrease in average magnitude at relatively low bias. Furthermore, even at the relatively low 200-mV bias, LBIC shows significant non-uniformity.

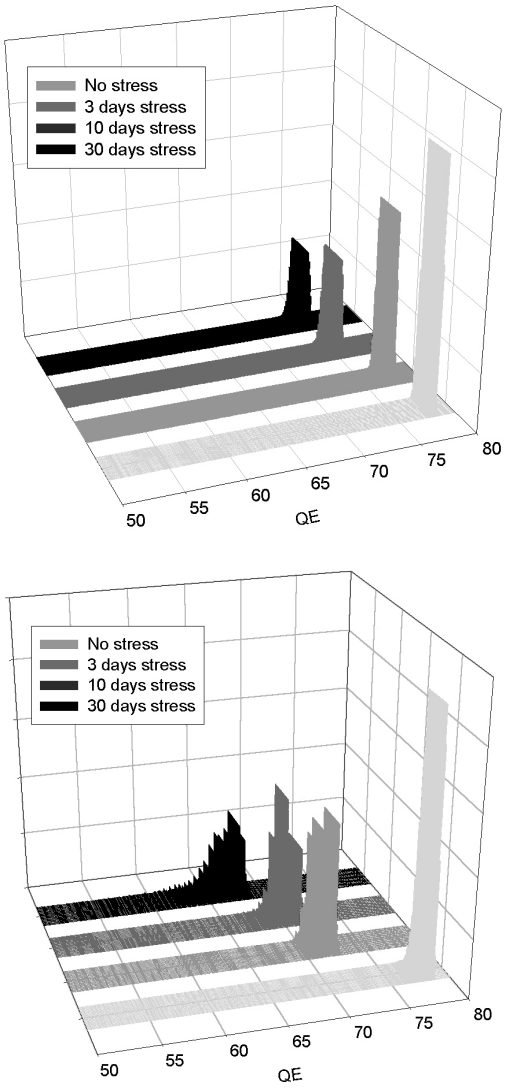

Fig. (6) Contrasting effect of stress on two CdTe cells made with and without a key contacting step

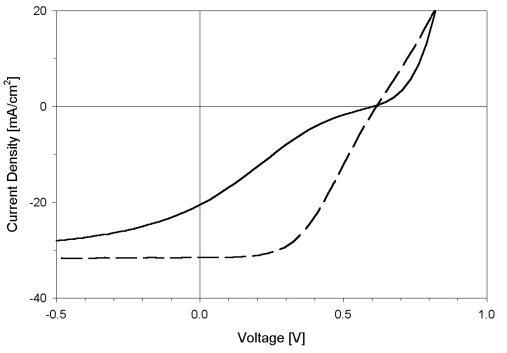

Fig. (7) J-V curve of a reasonably well-behaved CIGS cell (dashed) and a highly distorted one (solid)

5. Conclusions

LBIC has become a reliable tool for investigating a variety of solar-cell non-uniformities. It has become much more practical in recent years with improvements in translation stages, laser diodes, and data-handling techniques. LBIC is particularly valuable to help explain differences due to processing variations or changes induced by elevated-temperature stress. It can be reliably combined with other small-area investigation techniques to study the same area at different labs. Finally, in our experience, poorer performing cells almost always show larger LBIC variations indicative of poorer uniformity.

References

[1] J.D. Zook, R.B. Maciolik and J.D. Heaps, *Appl Phys. Lett.,* 37 (1980) 223-226.

[2] C.V. Hari Rao, H.E. Bates, and K.V. Ravi, *J. Appl. Phys.,* 47 (1976) 2614-2620.

[3] C. Belouet et al., "Growth and Characterization of Polysilicon Layers Achieved by the Ribbon-Against-Drop Process", in *Proc. 13th IEEE Photovolt. Spec. Conf.* (1978) 131-136.

[4] J.E. Phillips, R.W. Birkmire, and P.G Lasswell, "Stability of Thin-Film Cu_2S-Bassed Solar Cells", in *Proc. 16th IEEE Photovolt. Spec. Conf.* (1982) 719-722.

[5] S. Damaskinos, *Solar Cells,* 23 (1989) 151-156.

[6] R.J. Matson et al., "The Large-Scale Laser Scanner: Mill-Characterization o f Photovoltaic Cells and Modules", *Proc. 12th Euro. PVSEC* (1994) 1222-1225.

[7] W.D. Sawyer, *J. Appl. Phys.,* 59 (1986) 2361-2368.

[8] S.A. Galloway et al., *Appl. Phys. Lett.,* 68 (1996) 3725-3727.

[9] J.F. Hiltner and J.R. Sites, "High-Resolution Laser Stepping Measurements on Polycrystalline Solar Cells,"*Proc. 16 th Euro. PVSEC* (2000) 630-633.

[10] J.F. Hiltner and J.R. Sites, *Proc. Mat. Res. Soc.*, 668 (2001) H9.8.1-6.

[11] K. Durose. et al., *Prog. Photovolt: Res. Appl.,* 12 (2004) 177-217.

[12] J. Martin et al., *Prog. Photovolt: Res. Appl.,* 12 (2004) 283-295.

[13] C.R. Corwine et al., *Solar Energy Mat. Solar Cells,* 82 (2004) 481-489.

[14] J.R. Sites, H. Tavakolian and R.A. Sasala, *Solar Cells,* 29 (1990) 39-48.

This article was reviewed at Department of Physics, Faculty of Science, La Trobe University, La Trobe, AUSTRALIA, School of Applied Sciences, University of Technology, Baghdad, IRAQ, and Department of Physics, College of Education, The Iraqi University, Baghdad, IRAQ

Qusay A.H. Al-Naser

Department of Electrical and Electronic Engineering, University of Technology, Baghdad, IRAQ

Development of NVD's Using XR5™ IIT Technique and III-V Photocathode Under Night Sky Conditions

Image intensifier system (IIS) or night vision devices (NVD) are the imaging systems built up by using an image intensifier tube consisting of a photocathode, an anode in form of a phosphorous screen, and other optional components. Spectral sensitivity of the IIS depends on design but generally IIS used for external surveillance conditions are sensitive to radiation from (400 to 800) nm and sometimes up to 900nm. In this work the technical specifications of XR5™ image intensifier is used under different night sky conditions to evaluate the distance of vision for the NVD. Photocathodes have been developed using III-V materials with different concentrations; such materials have very high sensitivity in the near-infrared spectral region. The longest distance vision of (2120, 656) m can be obtained at full moon of 0.1 lux.

Keywords Night Vision Devices, Photocathode, Image intensifier system, XR5™
Received: 28 September 2011, **Revised**: 20 October 2011, **Accepted**: 27 October 2011

1. Introduction

The night vision devices (NVD) are used to enhance visual capability during low light level (night) activities as security, hunting, wildlife observation, boating, law enforcement, etc. Night vision can work in two very different ways, depending on the technology used – image enhancement or thermal imaging. Image enhancement works by collecting the tiny amounts of light, including the lower portion of the infrared light spectrum, that is exist but may be imperceptible to our eyes, and amplifying it to the point that we can easily observe the image. Thermal imaging operates by capturing the upper portion of the infrared light spectrum, which is emitted as heat by objects instead of simply reflected as light. Hotter objects, such as warm bodies, emit more of these light cooler objects like trees or building [1]. The NVD are basically composed of optical system (objective) which projects an image onto the photocathode of an image intensifier tube (IIT) which in its turn produces a light intensified image that is viewed through another optical system (ocular). All of these modules including the needed for IIT electrical power supply are mounted in some mechanic construction as a complete (and usually portable) device. Depending on the optical magnification and application area there are different types of night vision devices – night vision goggles, night vision binoculars and monoculars, night vision digital cameras (still or video), night vision sights, etc. The device parameters resolution, field of view, brightness gain, distortion, eyepiece dioptric adjustment, objective focus range, mechanical adjustments, weight, center of gravity, distance vision, price, etc., influence NVD performance [2].

2. Night Vision and External Surveillance Conditions

Ambient night illumination, atmospheric transmittance, contrast between the background and surveillance target and surveillance target type are affected as an external surveillance conditions on the NVD performance. The local weather patterns and an understanding of the effects on NVD performance are important for successful night vision observing [3]. The influence of the external surveillance conditions on the NVD performance can be described shortly as follows:

(i) Ambient night illumination

The visibility through the NVD is significantly affected by the illumination levels. The current night vision enhancement technology development has significantly improved the needed light-level requirements and the operational light level depends on the used image intensifier tube type [4]. The night vision technology using available light intensifying relies on the ambient light (starlight, moonlight, or sky glow from distant man-made sources, such as city lights, etc.) [5].

(ii) Atmospheric transmittance

Atmospheric conditions and consistence directly reflects to the air transmittance which is important factor to the image enhancement night vision technology [6]. Depends on the surface terrain and the surroundings, air temperature, atmospheric pressure, relative humidity, number and size

distribution of atmospheric aerosols, concentration of abnormal atmospheric constituents in the optical path such as smoke, dust, exhaust fumes, and chemical effluents, and refractive indices of all types of aerosol in the optical path [7].

(iii) Contrast between the background and surveillance target

The contrast between the background and surveillance target is important to correctly interpret the NVD image. Any terrain that contains varying albedos (forests, cultivated fields, etc.) will likely increase the level of contrast in a NVD image [3]. Monochromatic contrast difference between the integrated target and background Intensities [5].

3. Experimental Work

3.1 The III-V Photocathode

The main components for III-V are GaAs and InP, which can be alloyed with other materials such as Al and Sb, to give rise to ternary or quaternary compounds, like $Al_xGa_{1-x}As$ or $In_xGa_{1-x}As_yP_{1-y}$. These compounds allow for a large flexibility in the design of devices, and therefore it can be used in different applications. The $III_{1-x}III_xV$ or $IIIV_yV_{1-y}$ ternary alloys can be formed, where x and y are indices with values between 0 and 1. The lattice parameter and the band-gap energy of the alloy can be modified by varying the value of x or y. Photocathode has a very high sensitivity in the spectral region of about (450 to 950) nm (visible and near-infrared region). At night there is more light energy available in the near-infrared region than in the visible region. Therefore, if a device claims a high photosensitivity, make sure to find out where in the spectrum this is measured. A high photosensitivity in the blue or visible region may not perform as well as another system with a lower overall photosensitivity, but a higher value in the near-infrared region. Since we can control the energy band gap through the change of the material concentration, so that we can get the wavelength we need. [9]

3.2 Theoretical estimation for NVD design stage

A NVD choice is usually based on some preliminary user requirements about the NVD performance parameters. The device distance vision (D*v*) is a function of the external surveillance conditions and that dependence should be considered when trying to make a smart choice [8]. Using "Energy Calculations Method" (ECM), a formula for theoretical estimation of the NVD distance vision (D_v) is proposed (in m) [10]:

$$D_v = \sqrt{\frac{0.07 D_{in} f_{o'o} \tau_o \tau_a S_\Sigma \delta E A_{o'o} K}{M \varphi_{\min,ph}}} \qquad (1)$$

where D_{in} is the diameter of the objective inlet pupil (n m) f_{ob} is objective focal length (n mm) τ_o is objective transmittance dimensionless parameters, τ_a is atmosphere transmittance dimensionless parameters, S_Σ is Image Intensifier Tube (IIT) luminous sensitivity (n A/lm) δ is IIT limiting resolution (n lp/mm) *E is* ambient light illumination (n lux) A_{ob} is target (surveillance object) area (n m^2), K is contrast dimensionless parameters, M is signal-to-noise ratio of IIT (dimensionless parameter) $\varphi_{min.ph}$ is (IIT) photocathode limiting light flow (in lm)

The XR5^{TM} Image Intensifier enables the user to see even more during a full 24-hour day/night operation. This is done by the use of a fully integrated Auto-Gating unit, which controls the image not only during day-night-day transitions but also during dynamic lighting conditions such as those experienced. The XR5^{TM} IIT reveals more details of the night offers extend range capabilities with specifications of (S_Σ at 2850K = 0.0008 A/lm, δ = 72 lp/mm, M (@108µlux) = 28, $\varphi_{min.ph} = 4.10^{-13}$). *Din* = 0.018m, f_{ob} = 26mm, τ_o = 0.8.

External surveillance conditions are: (atmosphere transmittance (τ_a) = 0.8, Contrast (K) = 0.3, target (standing man) area (A_{ob}) m^2 = 1.425m^2). The expected distance vision D_v under different night sky conditions are shown in table (1).

Table (1) Distance vision at different night ky condition

external surveillance conditions	ambient light illumination (*E*) lux (*Night Sky Conditions*)	distance vision(D_v) (m)
Set 1	Full Moon: 0.1	2120,656
Set 2	half Moon: 0.05	1499.530
Set 3	Quarter Moon: 0.01	670,610
Set 4	Clear Starlight:0.001	212,065
Set 5	Overcast Starlight: 0.0001	67.061

4. Results and Discussion

Figure (1) indicates un area that NVD should be cover and vision clearly viewed when such a device used. We notice at different night sky conditions, the largest area can be covered through NVD at full moon i.e. (0.1 lux) was 46.40% from the whole area

that should seen, and become decreasing gradually and reach its lowest value of 1.47% at overcast starlight of 0.0001 lux. Figure (2) indicates the relation between the distances of visions compared with different night sky conditions. The longest distance vision of (2120, 656) m can be obtained at full moon of 0.1 lux. The new XR5^{TM} is the best choice to maintain combat effectiveness under all circumstances. In general, the higher the density of light, the better the NVD image quality.

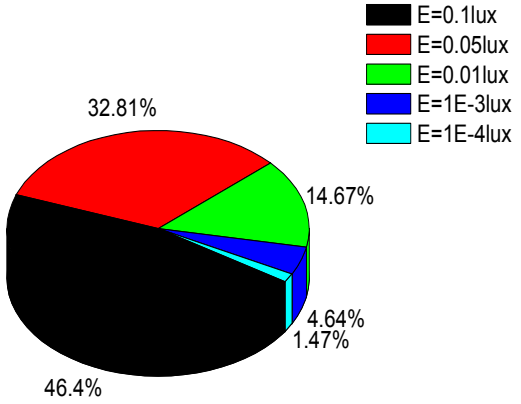

Fig. (1) NVD capabilities to cover the target area under different night sky conditions

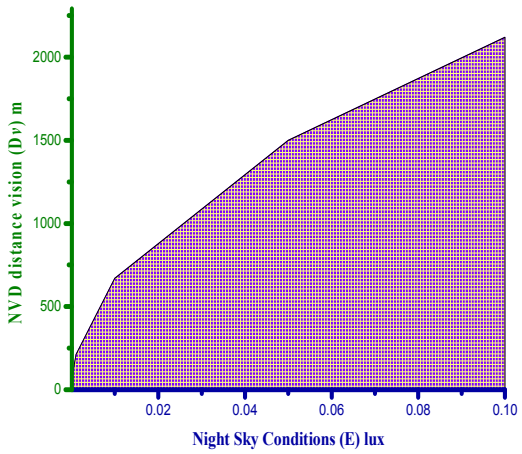

Fig. (2) NVD distance vision as a function of night sky conditions

To make photocathode more sensitive to spectrum in the near-infrared region, several III-V materials can be adjusting their concentrations to work in that region, as explained in table (2) In our work, choosing the wavelength of 800nm to work on, and energy band gap of the III-V components of 1.55eV were depended.

Table (2) The III-V components with E_g=1.55eV

Component	Concentration% (x)
$Al_xGa_{1-x}As$	11
$Al_xIn_{1-x}As$	48
$Al_xIn_{1-x}Sb$	72
$Al_xGa_{1-x}Sb$	60
$Ga_xIn_{1-x}P$	31
$Al_xIn_{1-x}P$	9
$GaAs_xP_{1-x}$	89

Components in table can be used instead of GaAs. When an Image Intensifier is used in really dark conditions the quality of the picture on the phosphor screen drops dramatically. Its overall brightness level falls and individual scintillations, tiny flashes of light, become more clearly visible. Such a picture is said to be 'noisy' and we describe this situation as being 'information-limited'. The only way to improve any image that shows signs of information-limiting is to increase the number of photons used to create an image.

A few of the basic problems of being seen at very low light levels are so fundamental to the physical state of darkness that they can only ever be overcome by the use of active illumination, being visible. At night, some 70% of light is in the near-infrared spectrum. The appearance of semi-visible/visible illumination overcomes this problem and users should consider having some sort of IR illuminator available to assist the Intensifier when climatic or lighting conditions restrict its performance. Only III-V materials are sensitive to be used with truly visible IR illuminators. The use of IR illuminators is the most cost effective way of getting higher increase in Intensifier performance.

5. Conclusions

The night vision device distance vision is directly influenced by the night sky conditions. Nevertheless if the distance vision is the most important parameter to consider or not the user should be aware of the expected distance vision values. It makes sense to take into account the worst possible night sky conditions when making the choice to guarantee the minimum NVD performance. The best NVD performance under these conditions obtained at full moon of 0.1 lux and become more difficult to recognize the target at the starlight overcast of 0.0001 lux, but still seen in the full darkness with a distance vision of (67.061) m at starlight overcast i.e. (0.0001 lux) because of the XR5^{TM} IIT technique has unprecedented performance for any environment

and any circumstance. The best distance vision can be obtained of (2120.656) m at 0.1lux. Although, III-V materials are more flexible choosing the energy band gap in which the wavelength can be specified for the region to work on.

References

[1] Daniela Borissova and Ivan Mustakerov, "Multicriteria Choice of Night Vision Devices Considering the Impact of Their Performance Parameters", AMO - Advanced Modeling and Optimization, Volume 10, Number 1, 2008.

[2] H. Lee Task, "Night Vision Devices and Characteristics", Visual Problems in Night Operations (pp. 7-1 - 7-8). Neuilly Sur Seine, France: NATO Advisory Group for Aerospace Research & Development. (NTIS No. AGARD-LS-187), 1992.

[3] "Night Vision Goggles – Helicopters", Civil Aviation Advisory Publication, Oct. 2007, CAAP 174-1(1).

[4] Pinkus, H.L. Task, "Measuring Observers' Visual Acuity through Night Vision Goggles", Air Force Research Laboratory, Human Effectiveness Directorate, ASC98-1884. 1998.

[5] Daniela Borissova, Ivan Mustakerov, "A Multicriteria Approach to Exploring Combinations of External Surveillance Conditions Defining a Given NVD Working Range Value", Bulgarian Academy of Sciences, Cybernetics and Information Technologies, Volume **9**, No. 4, Sofia, 2009.

[6] "Night Vision Goggles in Civil Helicopter Operations", Aviation Research Report, B2004/0152, April 2005.

[7] Cyrus M. Smith, "Detection of Special Operations Forces Using Night Vision Devices", U.S. Department of Energy, September 2001.

[8] Daniela Borissova, "Night Vision Devices Choice Taking into Account the External Surveillance Conditions", AMO – Advanced Modeling and Optimization, Volume 10, Number 2, 2008.

[9] T. Steiner, Semiconductor Nanostructures for Optoelectronic Applications, United States of America, pp. (230, 234), Artech House, Inc., 2004.

[10] Daniela Borissova, Ivan Mustakerov, "A Working Distance Formula for Night Vision Devices Quality Preliminary Information", Bulgarian Academy of Sciences, Cybernetics and Information Technologies, Volume 6, No. 3, Sofia, 2006.

This article was reviewed at Faculty of Science, Alexandria University, Alexandria, EGYPT, Institute of Nano Electronic Engineering, University Malaysia Perlis, Kangar Perlis, MALAYSIA, and School of Applied Sciences, University of Technology, Baghdad, IRAQ

Iraqi Journal of Applied Physics

Subject Index 2005 2011

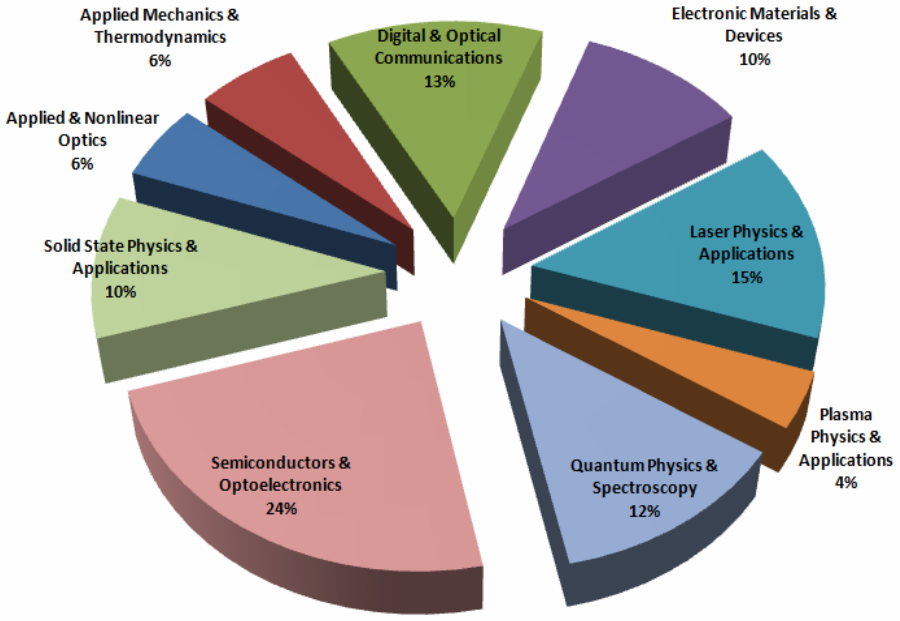

Applied & Nonlinear Optics

- Curvelet-Based Optical Flow Estimation Algorithm Based on Central Derivatives, 6(2), 13
- Design of a Multi-Electrode Immersion Lens for Ion-Optical Systems, 2(1,2), 27
- Development of an Inverted Optical Tweezers with Full Motional Control, 7(2), 19
- Investigations of Linear and Nonlinear Optical Properties of Transparent ZnO Thin Films Grown by Sol-Gel Method, 6(3), 29
- Key Mechanisms of the Nonlinear Amplification: Physics and Applications, 1(2), 3
- New Method for Calculating Cumulative Line Energy Using Pupil Function Technique, 2(1,2), 7
- Some Optical Properties of an Electrostatic Immersion Lens Using the Charge Density Method, 1(4), 21
- Temperature-Dependent Birefringence Properties of $Be_3Al_2Si_6O_{18}$ Crystal, L2(1), 12

Applied Mechanics & Thermodynamics

- Analytical Calculation of Heat Conduction in Two-Phase Heterogeneous Materials, 7(4), 11
- Characterization of D.C. Sputtering System, L1(1), 3
- Employing Inner Triplet Upgrade in Cold Mass Cooling Design for Large Hadron Collider, L2(1), 19
- HAZ Extent Analysis in Fiber-Reinforced Plastic Grooving by Laser, 1(1), 3
- Optimization Of Composition, Structure and Characteristics of Metal in Arc Deposition, 5(2), 37
- Marangoni Convection Effect on the Melting of GaSb/InSb/GaSb Sandwich Structured Sample, 4(2), 35
- Modeling of the Preheating Effect on Keyhole Laser Welding Efficiency, L1(1), 10
- Using Longitudinal Surface Acoustic Waves for Non-Destructive Testing of Inner Surfaces, L1(2), 9
- Torque and Magnetic Flux Analysis Using an Advanced Dynamic Dynamometer Test Bed for Electromechanical Motors, 5(1), 13

Digital & Optical Communications

- A CPW-Fed Printed Monopole Ultra-Wideband Antenna with E-Shaped Notched Band Slot, 6(4), 17
- A New Fractal Microstrip Bandpass Filter Design Based on Dual-Mode Square Ring Resonator for Wireless Communication Systems, 5(1), 7
- Analysis and Design of Combined Fractal Dipole Wire Antenna, 5(2), 29
- Classification of Digital Modulation Using Wavelet Transform, 1(3), 15
- Coherent Detection in Optical Fiber Systems, 3(1), 3
- Comparative Evaluation of Bit Error Rate in Frequency Selective Fading Channels Employed in Wavelet Modulation, L1(2), 14
- Design and Analysis of Special Small Size Cross Dipole Antenna, 6(2), 19
- Determination of The Satellite Images Orientation Using DCT Coefficients, 6(2), 31
- Dipole Antenna with Fractal Koch Curve Geometry for Multiple Frequency Applications, 7(2), 3
- Effect of Chirping on Received Pulse Shape in Optical Fiber Communications, L2(2), 7
- Linear Adaptive Antenna Array Geometry Effects on Radiation Pattern, L3(1), 3
- Novel Optical Fiber Sensor Based on SGMS Fiber Structure for Measuring Refractive Index of Liquids and Gases, 7(4), 17
- Performance Optimizing of Fourth Order Delta-Sigma Fractional-N Frequency Synthesizer using a Dither Technique for Third Generation (3G) Applications, 7(1), 3
- Phase Noise Compensation for Coherent Orthogonal Frequency Division Multiplexing in Optical Fiber Communications Systems, 5(2), 3

ISSN 1813-2065 Printed in IRAQ

Electronic Materials & Devices

Laser Physics & Applications

Plasma Physics & Applications

Quantum Physics & Spectroscopy

Semiconductors & Optoelectronics

Solid State Physics & Applications

* * *

- 1(1), 3 refer to IJAP, Vol. 1, No. 1, page 3
- L1(1), 3 refer to IJAPLett, Vol. 1, No. 1, page 3

* * *

 ISSN 1813-2065 Printed in IRAQ

Iraqi Journal of Applied Physics

Author Index 2005-2011

COPYRIGHT RELEASE
Iraqi Journal of Applied Physics (IJAP)

We, the undersigned, the author/authors of the article titled
……
……
……
……
……
……
that is presented to the Iraqi Journal of Applied Physics (IJAP) for publication, declare that we have neither taken part or full text from any published work by others, nor presented or published it elsewhere in any other journal. We also declare transferring copyrights and conduct of this article to the Iraqi Journal of Applied Physics (IJAP) after accepting it for publication.

The authors will keep the following rights:
1. Possession of the article such as patent rights.
2. Free of charge use of the article or part of it in any future work by the authors such as books and lecture notes without referring to the IJAP.
3. Republishing the article for any personal purposes of the authors after taking journal permission.

To be signed by all authors:

Signature:……..date: ……
Printed name: ……

Signature:……..date: ……
Printed name: ……

Signature:……..date: ……
Printed name: ……

Correspondence address:……...
……..
Address:……
……
……
Telephone:……..email: ……..

Note: Please complete and sign this form and mail it to the below address with your manuscript

The Iraqi Journal of Applied Physics
P. O. Box 55259, Baghdad 12001, IRAQ
Website: www.ijap.org, Email: editor@ijap.org
Phone: +964 7901274190

IRAQI JOURNAL OF APPLIED PHYSICS

Volume (7), Issue (4), October-December 2011

CONTENTS